Chapter 5

SUSPENSION MICROSTRUCTURES AND MECHANICS IN THE COLLOIDAL FILM DRYING PROCESS

5.1 Introduction

Colloidal suspensions find widespread applications in science and technology. They are commonly applied as thin films on a substrate to modify or enhance its surface properties. An example is latex paint, which, by changing the corrosion resistance and color of the substrate, makes the material more durable and aesthetically appealing. In addition to chemistry, the thin film structure and mechanics also become increasingly important to the film's quality and functionality, especially for many novel materials. For instance, the optical properties of thin-film colloidal structures are strongly influenced by its long-range crystalline nature [1] or lack thereof [2]. On the other hand, the residual stresses in the film can lead to cracking and warping that adversely affect the film quality [3–5]. The thin film structural and mechanical properties largely depend on the film drying process, where the solvent is removed from the suspension, and the colloidal particles are compressed by the receding interface [6]. A thorough understanding of this process is clearly necessary for further innovations [7, 8].

The colloidal film drying process is complex: in addition to the interfacial phenomena from the continuously receding liquid-air interface, such as capillary pressure and Marangoni flow [6, 9], it is also affected by features inherent to the colloidal suspension [10, 11]: (*i*) Brownian motion, (*ii*) hydrodynamic interactions, and (*iii*) interparticle potential. Both (*i*) and (*ii*) originate from the disparate size difference between the colloidal particles and the solvent molecules. Examples of (*iii*) include screened electrostatic potentials, excluded volume effects, and the plastic/elastic deformation of the particles [9]. These features are also strongly affected by the confinement from the interface and the substrate [10, 12–15]. Clearly, the complexity necessitates simplifications to distill the essential physics.

In this work we use Brownian Dynamics (BD) simulations and continuum models to study the structural and mechanical evolution of the colloidal film drying process. We focus on the simplest non-trivial model system: the uniaxial compression of monondisperse hard-sphere Brownian particles between hard boundaries without hydrodynamic interactions. This system captures the colloidal interactions among the moving boundary, the particle Brownian motion, and the excluded volume effect. Compared to earlier simulations of the film drying processes via kinetic Monte Carlo [16], soft potential BD [17], and multiscale methods [18–20], focusing on a simple model allows systematic investigation of key parameters. Indeed, our focus on simple systems is motivated by progress in the rheology of dense colloidal suspensions, which has come from in-depth investigations of hard-sphere Brownian systems [21–23].

In the colloidal film drying process, as the fluid evaporates, the liquid-air interface pushes the particles towards the stationary substrate, while the particle Brownian motion attempts to smooth out any local concentration fluctuations (see Fig. 5.1). With an interface velocity U_w, the competition between convection and diffusion defines Péclet number,

$$\mathrm{Pe}_U = aU_w/d_0, \tag{5.1}$$

where a is the particle radius and $d_0 = k_\mathrm{B}T/\zeta$ is the single-particle Stokes-Einstein-Sutherland diffusivity, with $k_\mathrm{B}T$ the thermal energy scale and $\zeta = 6\pi\eta_0 a$ the particle resistance in a solvent of viscosity η_0. Physically, $\mathrm{Pe}_U \ll 1$ suggests slow interface movement and Brownian motion dominated dynamics, while $\mathrm{Pe}_U \gg 1$ indicates fast interface movement and convection dominance. Experimentally, varying the drying rate changes Pe_U, which, in turn, alters the film structure. To obtain uniform and ordered film structures, conventional wisdom is that $\mathrm{Pe}_U \ll 1$ is necessary to allow time for the thermodynamic phase transition [24–26]. Surprisingly, recent experiments and simulations also found highly ordered structures with $\mathrm{Pe}_U \gg 1$ [27].

The first objective of this work is to characterize the film structures over a wide range of Pe_U. In the $\mathrm{Pe}_U \ll 1$ limit, the final film structure can be predicted from the equilibrium phase behaviors of confined suspensions, as the slow interface movement allows sufficient time for equilibration. The phase behavior of hard-sphere systems are well studied in experiments [28] and simulations [29, 30]. With confinement, the crystallization onset density is significantly reduced compared to bulk systems [31], and reducing the confinement (increasing the gap spacing) introduces a hierarchy of crystalline structures as $c\triangle \rightarrow c\square \rightarrow (c+1)\triangle$, where c is the number of crystalline layers, and $\triangle$ and $\square$ respectively represent crystalline structures of triangular and square symmetries (see Fig. 5.2). The behavior at finite Pe_U and large gap spacing may be inferred from the sedimentation process next to a confining boundary through a change of reference frame, assuming limited influences of hydrodynamic interactions. Experiments [32–34] and simulations [35–37] show that crystal growth is initiated next to the confining boundary as a first order phase transition, and continues upwards epitaxially. With increasing sedimentation velocity—equivalent to increasing the interface velocity in the drying process—the competition between the particle settling and the crystal growth lead to stack faults and even glassy structures in crystalline domains. Similar structural evolution is expected for the drying process near the moving interface. Furthermore, at smaller gap spacing, the confinement can disrupt the crystallization process, leading to frustrated structures [38, 39]. However, we are not aware of any similar theoretical and simulation investigations in the $\mathrm{Pe}_U \gg 1$ limit.

We deliberately limit ourselves to systems without hydrodynamic interactions. With this simplification, compression, filtration, and sedimentation are equivalent when the gap spacing are sufficiently large. However, such equivalence does not hold with hydrodynamic interactions. For example, Rayleigh-Taylor instability [34] develops in sedimentation as particles are under constant forces, but not in compression or filtration as particles move with the imposed flow. In sedimentation, the back flow from the no-flux boundary conditions leads to strong particle velocity fluctuations [40]. However, the back flow is absent in filtration and compression due to solvent removal. Furthermore, the influences of hydrodynamic interactions on confined systems are profound [12, 15], and are beyond the scope of this work.

The second objective of this work is to study the stress distributions in the suspension during the drying process. The residual stress can cause unwanted deformation in the film product, such as cracking and warping [4, 5, 9]. Physically, they are attributed to the capillary pressure from the liquid menisci among the colloidal particles. However, stress balance alone can show that the deformation is inevitable regardless of the underlying mechanisms. The argument goes as follows: a stable film formed by the drying process with interface movement in the z direction must satisfy the steady state stress balance $\partial \Sigma_{zz}/\partial z = 0$, suggesting that the zz component of the stress, Σ_{zz}, must be constant across the film. If the Σ_{zz} distribution in the z-direction is not constant, other mechanisms including the lateral film deformation must step in to maintain the constant stress. Therefore, monitoring the stress distribution during the compression process provides a key indication on future film deformation. This often overlooked aspect of the compression process is also addressed in this work.

The film drying process is also affected by the interface movement profile: in addition to the constant velocity movement, the interface may also move in response to a constant imposed normal stress Σ_e. The resulting film structural and mechanical evolution is also investigated in this work. Here, the competition between the external energy $a^3\Sigma_e$ and the thermal energy $k_B T$ defines a stress Péclet number

$$\mathrm{Pe}_\Sigma = a^3\Sigma_e/(k_B T). \tag{5.2}$$

With this drying process, the interface slows down as the suspension osmotic pressure grows due the increasing density, and eventually stops when the osmotic pressure matches Σ_e. Clearly, a single Pe_Σ corresponds to spectrum of Pe_U down to zero in the constant velocity drying process.

Experimentally, constant stress interface movement may be achieved by compressing the suspension using a rigid, porous substrate that is only permeable to the solvent with constant mechanical load. Although new for colloidal systems, this compression mode is common in the Surface Force Apparatus (SFA) experiments to characterize the molecular interactions in thin films [41]. These experiments lead to extensive molecular dynamics [42–45] and Monte Carlo [46, 47] investigations for interpreting the results. With the same principle of operation to SFA experiments, the constant normal stress compression is a promising method to characterize interactions in colloidal films. We hope this work serves as a first step for future investigations in this direction.

Another focus of this work is on continuum models, which are crucial for selecting parameters in the engineering and design of the drying process [26, 48]. Assuming local thermal equilibrium, these models are derived from the principle of mass conservation, and agree well with experiments with strong thermal fluctuations ($\mathrm{Pe}_U \ll 1$ or $\mathrm{Pe}_\Sigma \ll 1$). The same philosophy is used to model the sedimentation processes [10, 49, 50]. However, it is unclear if these continuum models remain valid when the thermal fluctuations are weak. In this limit, other physics also becomes important. For example, non-local effects are necessary to properly model the non-equilibrium flow of granular materials [51]. By developing continuum models for constant velocity and constant normal stress interface movement following the traditional approach [10], we compare the model predictions with the simulation results to elucidate the validity of the models, especially in the high Péclet number limit.

Finally, dynamic simulation of the drying process and the measurement of suspension stress profiles pose significant challenges for existing algorithms. Brownian dynamics algorithms for hard-sphere suspensions can be based on event-driven [52,

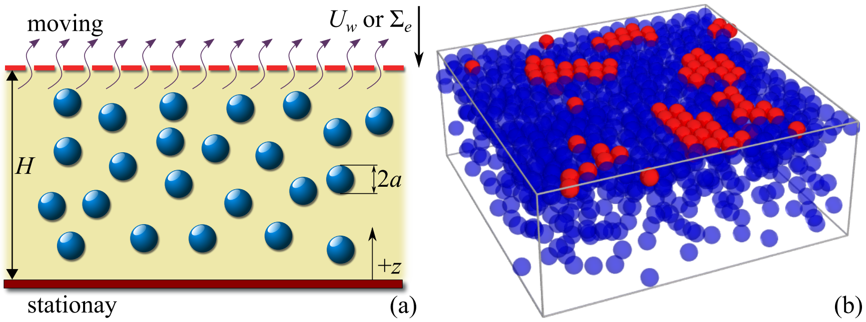

Figure 5.1: (Color online) (a): A sketch of the colloidal film drying process. Colloidal particles of radius a are sandwiched between a stationary substrate at $z = 0$ and an interface at $z = H$, moving either at constant velocity U_w or in response to a constant normal stress Σ_e in the $-z$ direction. The interface allows the solvent, but not the particles, to pass. (b): A snapshot of the simulation cell at $\mathrm{Pe}_U = 50$ and $H = 15a$. The blue particles are amorphous while the red particles are crystalline.

53] or time-discretization [21, 54–56]. Here, the complications due to the moving interface rules out the event-driven algorithms. On the other hand, time-discretization methods known as the "potential-free" algorithms are based on iterative overlap resolution. Unfortunately, they are unsuitable for accurate stress profile measurement, as the particle position changes in the overlap resolution process. Moreover, circular overlap resolution at high densities may halt the simulation. In this work, we address these challenges by developing a new Energy Minimization Potential-Free (EMPF) algorithm, which imposes the hard-sphere potential by simultaneously resolving the overlaps using the minimum energy principle.

This rest of the chapter is arranged as follows: in Sec. 5.2 we describe the problem setup, the energy minimization potential-free algorithm, and the continuum model. The simulation and numerical results are presented and discussed in Sec. 5.3. Finally, we summarize and conclude in Sec. 5.4.

5.2 Methods

We consider N neutrally buoyant colloidal particles of equal radius a suspended in a solvent of viscosity η_0, occupying a total volume of V. The position of particle i is at $\boldsymbol{x}_i = (x_i, y_i, z_i)$. The particle number density $n = N/V$ and the volume fraction $\phi = \frac{4}{3}\pi a^3 n$. The suspension is sandwiched between a stationary substrate at $z = 0$ and an interface at $z = H(t)$, moving towards the substrate in the $-z$ direction. The sketch of the colloidal film drying process is shown in Fig. 5.1a, and a snapshot of the simulation cell is shown in Fig. 5.1b. In the transverse (x- and y-) directions, we set the simulation cell width to W, *i.e.*, $V = HW^2$, and impose periodic boundary conditions.

At the beginning of the film drying process, the initial volume fraction is ϕ_0 and the interface is located at $z = H_0$. The colloidal particles are randomly distributed without overlapping between the two boundaries. For constant velocity interface movement, the interface position changes according to

$$\frac{\mathrm{d}H}{\mathrm{d}t} = -U_w, \tag{5.3}$$

where U_w is the interface speed. When the interface is subject to an external normal stress of magnitude Σ_e, its position changes according to the force balance

$$\zeta \alpha_m \frac{\mathrm{d}H}{\mathrm{d}t} = a^2 \Sigma_m(t) - a^2 \Sigma_e, \tag{5.4}$$

where $\Sigma_m(t)$ is the instantaneous suspension normal stress on the moving interface, and α_m is the interface resistance coefficient, *i.e.*, $\alpha_m \zeta$ is the hydrodynamic resistance of the interface. Eq. (5.3) and (5.4) suggest that $\mathrm{Pe}_U = \mathrm{Pe}_\Sigma / \alpha_m$ when $\Sigma_m = 0$. However, as the suspension osmotic pressure grows with ϕ, the equivalence quickly breaks down during the drying the process.

Without hydrodynamic interactions, the time evolution of particle position $\boldsymbol{x}_i$ follows the overdamped Langevin equation [21, 54, 57],

$$\zeta \frac{\mathrm{d}\boldsymbol{x}_i}{\mathrm{d}t} = \boldsymbol{f}_i^{\mathrm{P}} + \boldsymbol{f}_i^{\mathrm{W}} + \boldsymbol{f}_i^{\mathrm{B}}, \tag{5.5}$$

where $\zeta = 6\pi\eta_0 a$, $\boldsymbol{f}_i^{\mathrm{P}}$ and $\boldsymbol{f}_i^{\mathrm{W}}$ are respectively the forces from the interparticle and the particle-wall potentials, and $\boldsymbol{f}_i^{\mathrm{B}}$ is the Brownian force satisfying $\overline{\boldsymbol{f}_i^{\mathrm{B}}(t)} = 0$ and $\overline{\boldsymbol{f}_i^{\mathrm{B}}(t)\boldsymbol{f}_j^{\mathrm{B}}(t')} = 2k_{\mathrm{B}}T\zeta^{-1}\delta_{ij}\delta(t-t')\mathbf{I}$ with δ_{ij} the Kronecker delta, $\delta(t-t')$ the Dirac delta, and $\mathbf{I}$ the idem tensor. The interparticle potential V_{ij}^{P} and the particle-wall potential V_i^{W} are respectively

$$V_{ij}^{\mathrm{P}} = \begin{cases} 0, & \text{if } r_{ij} > 2a \\ \infty, & \text{otherwise} \end{cases} \text{ and } V_i^{\mathrm{W}} = \begin{cases} 0, & \text{if } a < z_i < H - a \\ \infty, & \text{otherwise} \end{cases}, \tag{5.6}$$

where $r_{ij} = \|\boldsymbol{x}_i - \boldsymbol{x}_j\|$. Computation of $\boldsymbol{f}_i^{\mathrm{P}}$ and $\boldsymbol{f}_i^{\mathrm{W}}$ via the EMPF algorithm for hard potentials is discussed next.

The Energy Minimization Potential-Free algorithm

The potential-free BD algorithm directly discretizes Eq. (5.5) with time step Δt for suspensions with singular hard-sphere potentials and advances the simulation following a predictor-corrector scheme. The position of particle i changes as

$$\boldsymbol{x}_i(t + \Delta t) = \boldsymbol{x}_i(t) + \Delta \boldsymbol{x}_i^{\mathrm{R}} + \Delta \boldsymbol{x}_i^{\mathrm{P}}. \tag{5.7}$$

In the predictor step, the particles are randomly displaced by $\Delta \boldsymbol{x}_i^{\mathrm{R}}$, drawn from a normal distribution with zero mean and a variance of $2d_0\Delta t$, with $d_0 = k_{\mathrm{B}}T/\zeta$. In the corrector step, the algorithm ensures that the suspension is free from any overlaps by moving particle i a distance $\Delta \boldsymbol{x}_i^{\mathrm{P}}$, such that for any $i \neq j$, $\|\boldsymbol{x}_i - \boldsymbol{x}_j\| \geq (a_i + a_j)$. The resulting interparticle force is $\boldsymbol{f}_i^{\mathrm{P}} = \zeta_i \Delta \boldsymbol{x}_i^{\mathrm{P}}/\Delta t$, with $\zeta_i = 6\pi\eta_0 a_i$. The stress tensor for homogeneous suspensions is simply the spatial moment of the interparticle force, $\boldsymbol{\Sigma} = -V^{-1}\sum_{i=1}^{N} \boldsymbol{x}_i \boldsymbol{f}_i^{\mathrm{P}}$.

In the original potential-free algorithm, the overlap-free condition is satisfied by repeatedly restoring the overlapping pairs back to contact along their line of centers until the system is free of overlaps. As soon as the algorithm identifies an overlapped pair $s = (p, q)$ with particles p and q, it moves each particle a distance $\Delta \boldsymbol{x}_{s,p}^{\mathrm{P}}$ and $\Delta \boldsymbol{x}_{s,q}^{\mathrm{P}}$ to meet the non-overlapping condition and Newton's third law, $\boldsymbol{f}_{s,p}^{\mathrm{P}} + \boldsymbol{f}_{s,q}^{\mathrm{P}} = 0$. The algorithm works efficiently for dilute suspensions. However, for dense suspensions, the original algorithm suffers several issues: (*i*) performance degradation. Resolving the overlap of one pair may cause secondary overlaps in adjacent particles. Therefore, computationally expensive iterative overlap resolution that scans the entire suspensions multiple times are necessary. In extreme cases, the simulation may be trapped by a repeating sequence of configurations and unable to advance in time. The confining boundaries in the film drying process further aggravate this problem. (*ii*) indeterminate terminal configurations. For particles with multiple overlaps with other particles, the final overlap-free configuration strongly depends on the order in which the overlap pairs are resolved. (*iii*) ambiguous local stress. As the stress is the spatial moment of the interparticle force, the local stress is ambiguous if a particle has multiple overlaps with other particles: it is unclear which particle position during the overlap resolution process should be used for stress measurement. This is especially problematic for measuring the stress profile in suspensions with large stress variations.

Here, we develop the Energy Minimization Potential-Free (EMPF) algorithm to address these issues. The motivation for the EMPF algorithm is the realization that, for an overlapping pair, the particle movement from the original potential-free algorithm minimizes the energy cost. In other words, for an overlapping pair $s = (p, q)$, it minimizes

$$\epsilon_s = \epsilon_p + \epsilon_q = \boldsymbol{f}_p^{\mathrm{P}} \cdot \Delta \boldsymbol{x}_p^{\mathrm{P}} + \boldsymbol{f}_q^{\mathrm{P}} \cdot \Delta \boldsymbol{x}_q^{\mathrm{P}}, \tag{5.8}$$

subject to the non-overlapping and zero total force constraints,

$$\|(\boldsymbol{x}_p + \Delta \boldsymbol{x}_p^{\mathrm{P}}) - (\boldsymbol{x}_q + \Delta \boldsymbol{x}_q^{\mathrm{P}})\| - (a_p + a_q) = 0, \tag{5.9}$$

$$\boldsymbol{f}_p^{\mathrm{P}} + \boldsymbol{f}_q^{\mathrm{P}} = 0. \tag{5.10}$$

It can be shown that the $\Delta \boldsymbol{x}_p^{\mathrm{P}}$ and $\Delta \boldsymbol{x}_q^{\mathrm{P}}$ that minimize ϵ_s are unique—a manifestation of the minimization principle in classical mechanics [58]. The idea of energy minimization is also used by O'Hern et al. [59] to generate jammed packings.

The EMPF algorithm *simultaneously* removes multiple overlaps by generalizing the minimization argument for particles pairs, and therefore resolves the issues associated with the original potential-free algorithm. For a overlapped cluster with n particles and m overlapping pairs, the non-overlapping configuration can be found by minimizing the following cost function:

$$\begin{aligned} f_c(\boldsymbol{y}) = \sum_{s=1}^{m} \lambda_s^p [\|(\boldsymbol{x}_p + \Delta \boldsymbol{x}_p^{\mathrm{P}}) - (\boldsymbol{x}_q + \Delta \boldsymbol{x}_q^{\mathrm{P}})\|^2 - (a_p + a_q)^2] \\ + \boldsymbol{\lambda}^f \cdot \sum_{i=1}^{n} \boldsymbol{f}_i^{\mathrm{P}} + \sum_{i=1}^{n} \epsilon_i, \end{aligned} \tag{5.11}$$

where $\epsilon_i = \boldsymbol{f}_i^{\mathrm{P}} \cdot \Delta \boldsymbol{x}_i^{\mathrm{P}}$ is the energy for moving particle i, λ_s^p is the Lagrange multiplier associated with the pair $s = (p, q)$, $\boldsymbol{\lambda}^f = (\lambda_x^f, \lambda_y^f, \lambda_z^f)$ is the three-component Lagrange multiplier vector associated with the zero total force constraint, and $\boldsymbol{y} = (\{\Delta \boldsymbol{x}_i^{\mathrm{P}}\}_n, \{\lambda_s^p\}_m, \boldsymbol{\lambda}^f)$ is the unknown vector. The minimum of f_c in Eq. (5.11) is found by solving the non-linear systems of equation $\boldsymbol{\nabla}_{\boldsymbol{y}} f_c = 0$ using Newton-Raphson iterations. The analytical Hessian matrix, $\mathbf{H}(f_c) = \boldsymbol{\nabla}_{\boldsymbol{y}} \boldsymbol{\nabla}_{\boldsymbol{y}} f_c$, is used as the Jacobian for the solver. The associated linear systems are solved using dense linear solvers for small clusters ($n < 50$), and sparse solvers otherwise.

In dynamic simulations with the EMPF algorithm, after applying the random displacement $\Delta \boldsymbol{x}_i^{\mathrm{R}}$, clusters with overlaps are first identified, and the overlaps in one cluster are then resolved simultaneously. At high density, particles from different clusters may create new overlaps after a resolution. In this case, these clusters are merged into a new one for simultaneous overlap resolution based on the current configuration to ensure the overlap-free configuration. The cluster merge continues to ensure that all the overlaps in the current configuration are resolved simultaneously. In the case of solver failure, a new set of random displacements $\Delta \boldsymbol{x}_i^{\mathrm{R}}$ is applied for all particles from the last non-overlapping configuration. We stop after successive solver failures, providing an exist point for the simulations.

Several comments are in line for the EMPF algorithm. First, the simultaneous overlap resolution is consistent with pairwise interactions. Since the algorithm always lead to particle clusters in mechanical equilibrium, pairwise force decomposition is always possible [58]. Second, to resolve issues associated with the original potential-free algorithm, the EMPF algorithm requires solving a system of nonlinear equations. The computation efficiency may be improved by techniques such as parallelization, which are not available for sequential pairwise overlap resolution. The EMPF algorithm compared to the original algorithm is like the Newton-Raphson method compared to the successive substitution in root-finding problems: the former is always preferred due to its reliability and robustness. Finally, the EMPF algorithm, like many methods based on time discretization, overestimates the contact value in the singlet and pair distribution functions [52], and exhibits a slow $\sqrt{\Delta t}$ error convergence [60]. Therefore, small time steps are necessary for meaningful results. We have checked that the EMPF algorithm produces correct results in the pair distribution functions, osmotic pressure, and stress correlation functions in equilibrium bulk suspensions. The results are also insensitive to the system sizes.

Eq. (5.11) is valid for clusters not in contact with the confining boundaries. To study the film drying processes, cost functions that account for the particle-wall interactions under different interface movement profiles are also necessary. These are presented in the appendix. With constant velocity interface movement, Eq. (5.3) alone is sufficient. For constant normal stress interface movement, Eq. (5.4) becomes

$$H(t+\Delta t) = H(t) - a^2 \Sigma_e \Delta t / (\zeta \alpha_m) + \Delta H^{\mathrm{P}}, \tag{5.12}$$

where the second term in the right hand side accounts for the wall movement from the imposed stress, and ΔH^{P} is the interface's response to the suspension stresses. It is determined by minimizing the associated cost functions.

The continuum model

The continuum transport model for the film drying process is inspired by earlier colloidal theories [10, 26, 48, 50]. The influences of the solvent are ignored as hydrodynamic interactions are not considered. The concentration gradient introduced by the moving interface exerts a mean Brownian force $\boldsymbol{f}^{\mathrm{B}}$ on the particles, which in turn move at a mean Brownian velocity $\boldsymbol{u}^{\mathrm{B}} = \boldsymbol{f}^{\mathrm{B}}/\zeta$. The Brownian force arises from the chemical potential gradient, *i.e.*, $\boldsymbol{f}^{\mathrm{B}} = -\boldsymbol{\nabla}\mu$, and the change of μ follows $\mathrm{d}\mu = v\mathrm{d}\Pi$ for isothermal systems, where $v = n^{-1} = \frac{4}{3}\pi a^3/\phi$ is the particle specific volume, and Π is the local osmotic pressure. With the assumption of local thermal equilibrium, the osmotic pressure $\Pi(\phi) = Z(\phi)n(\phi)k_{\mathrm{B}}T$ with $Z(\phi)$ the compressibility. The Brownian velocity is therefore $\boldsymbol{u}^{\mathrm{B}} = -d_0\phi^{-1}[\phi Z(\phi)]'\boldsymbol{\nabla}\phi$ and the volumetric flux is $\boldsymbol{j}_\phi = \phi\boldsymbol{u}^{\mathrm{B}}$, with the prime denoting derivative. Conservation of local flux in the z-direction leads to an equation of $\phi(z,t)$,

$$\frac{\partial\phi}{\partial t} = \frac{\partial}{\partial z}\left\{d_0\frac{\mathrm{d}}{\mathrm{d}\phi}[\phi Z(\phi)]\frac{\partial\phi}{\partial z}\right\}. \tag{5.13}$$

The boundary conditions are

$$\frac{\partial\phi}{\partial z} = 0 \text{ at } z = 0, \tag{5.14}$$

$$-d_0\frac{\mathrm{d}}{\mathrm{d}\phi}[\phi Z(\phi)]\frac{\partial\phi}{\partial z} - \phi\frac{\mathrm{d}L}{\mathrm{d}t} = 0 \text{ at } z = L(t), \tag{5.15}$$

where the interface motion $L(t)$ is determined by its movement profile. The initial condition is $\phi(z,0) = \phi_s$, *i.e.*, a uniform starting density in the gap between $z = 0$ and $z = L(0) = L_0$. Note that L in the model refers to the gap spacing accessible to the particles, and H in the simulations is the distance between the two confining boundaries. In the appendix, we discuss the conversion between H and L for proper comparison between the model and the simulations. When the interface moves at a constant velocity U_w,

$$L(t) = L_0 - U_w t, \tag{5.16}$$

and when the interface is subject to a constant external stress Σ_e, the change in $L(t)$ follows Eq. (5.4), as

$$\zeta\alpha_m\frac{\mathrm{d}L}{\mathrm{d}t} = \frac{3k_{\mathrm{B}}T\phi Z(\phi)}{4\pi a} - a^2\Sigma_e, \tag{5.17}$$

with ϕ evaluated at $z = L(t)$.

Here, we choose the Le Fevre equation of state [61] for $Z(\phi)$,

$$Z(\phi) = \frac{1+\alpha_3\phi}{(1+\alpha_1\phi)(1+\alpha_2\phi)(1+\beta_1\phi+\gamma_1\phi^2)(1+\beta_2\phi+\gamma_2\phi^2)}, \tag{5.18}$$

with the coefficients α_k, β_k and γ_k (k = 1,2,3) presented in Table 5.1. Eq. (5.18) has a simple pole at $\phi = -\alpha_1^{-1} = 0.6366$ and is reasonably accurate at both low and

Table 5.1: The coefficients associated with the Le Fevre equation of state in Eq. (5.18) from Le Fevre [61].

k	α_k	β_k	γ_k
1	−1.5708	−2.9552	2.5521
2	1.0232	−1.3795	2.1339
3	−0.8824		

high densities [62]. Selecting a single equation of state for all densities implies that the model ignores phase transitions and greatly simplifies the solution procedure. Further details on solving the continuum model are also presented in the appendix.

5.3 Results and Discussions

To investigate the colloidal film drying process, we carry out a series of BD simulations using the EMPF algorithm with constant velocity and constant normal stress interface movement. Each simulation contains $N = 1000$ particles, and starts with an initial gap width $H_0 = 30a$ and an initial volume fraction $\phi_0 = 0.1$. For constant normal stress interface movement, the interface resistance coefficient $\alpha_m = 1$. In the simulations, we scale the length with a and the time with a^2/d_0 when $\mathrm{Pe}_U \leq 1$ and $\mathrm{Pe}_\Sigma \leq 1$, and with a/U_w for $\mathrm{Pe}_U > 1$ and $\zeta/(a\Sigma_e)$ for $\mathrm{Pe}_\Sigma > 1$. The dimensionless step size is 10^{-4}. The simulations terminate after 20 successive solver failures. We perform 300 simulations for each Péclet number and present the averaged results unless otherwise stated. In what follows, we present the results with constant velocity and constant normal stress together and highlight their differences.

Interface movement

When the interface moves at a constant velocity U_w, Fig. 5.2 shows the average gap width H at which the simulations terminate as a function of Pe_U. Here, a simulation terminates because the suspension structures created by the approaching confining boundaries cannot be relaxed by the particle thermal or mechanical fluctuations, *i.e.*, the suspension jams, leading to repeated solver failures. In Fig. 5.2, the terminal H increases with the growing Pe_U, and is more sensitive to Pe_U when $\mathrm{Pe}_U \gg 1$. Meanwhile, the variations among different simulations also grow significantly with Pe_U. The inset of Fig. 5.2 presents the terminal H as a function of ϕ on the drying operating curve $H(\phi)$ over the phase diagram of Fortini and Dijkstra [30] for confined hard-sphere suspensions. The phase diagram outlines the boundaries of different crystalline structures in the H-ϕ plane. For example, $4\triangle$ means four-layer crystalline

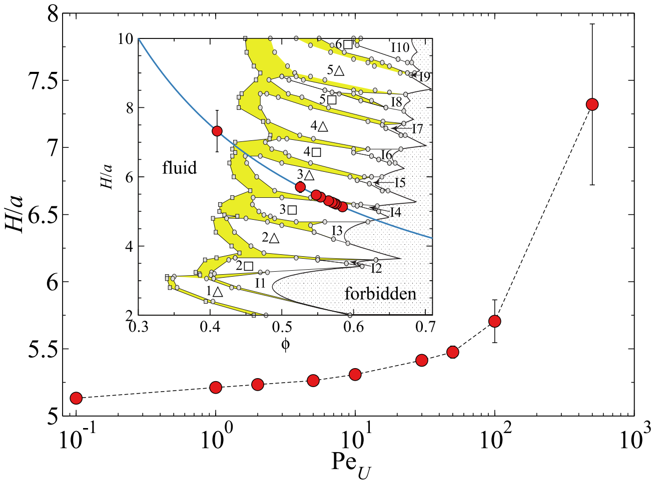

Figure 5.2: (Color online) The terminal gap width H as a function of Péclet number Pe_U for constant velocity interface movement. The error bars corresponds to variations in 300 independent simulations. The inset shows the gap width H as a function of the volume fraction ϕ for the initial H_0 and ϕ_0 in the simulations. The $H(\phi)$ operating curve is superimposed over the H-ϕ equilibrium phase diagram of confined hard-sphere systems from Fortini and Dijkstra [30] (with permission). The terminal gap widths in the simulations are also shown as circles in the inset.

structures with triangular symmetry. In the phase diagram, regions with crystalline-fluid coexistence are shown in yellow, and intermediate structures are tagged with letter 'I' followed by an integer. On the right, the shaded areas are geometrically inaccessible for any configurations. The operating curve is a hyperbola determined by the initial conditions H_0 and ϕ_0, satisfying $H\phi = H_0\phi_0$. Note that the $H(\phi)$ operating curves are identical for both modes of interface movement. As mentioned in the introduction, traversing the operating curve on the phase diagram provides valuable information on the film structures in the near equilibrium, $\mathrm{Pe}_U \ll 1$, limit.

When $\mathrm{Pe}_U \ll 1$, Brownian motion readily relaxes structural heterogeneities due to the moving interface, and gives rise to a roughly uniform structure across the gap. In the quasi-equilibrium limit ($\mathrm{Pe}_U \to 0$), we expect the simulation to terminate in the geometric limit, which, according to the inset of Fig. 5.2, is $H \approx 4.8a$. In the simulations, however, the terminal H at $\mathrm{Pe}_U = 0.1$, $H = 5.13a$, is far from the geometric limit and is closer to the phase transition between the 3△ phase and the 3□ phase. The slow interface movement at $\mathrm{Pe}_U = 0.1$ still disrupts the structural transitions, and eventually terminates the simulation by creating geometric frustrations. At $\mathrm{Pe}_U \sim 1$, the terminal H is also close to the 3△ and 3□ transition in

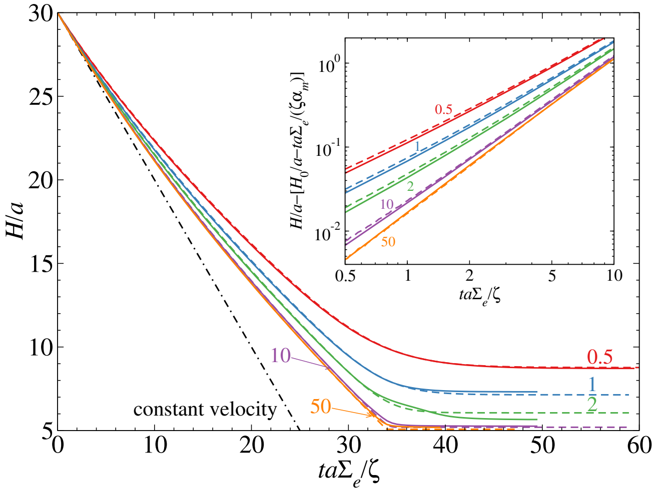

Figure 5.3: (Color online) The interface position H/a as functions of the scaled time $ta\Sigma_e/\zeta$ for constant normal stress interface movement with $\mathrm{Pe}_\Sigma = 0.5$, 1, 2, 10, and 50, annotated in the figure with the same color as the curve. Solid lines are simulation results and dashed lines are from the continuum model. The dash-dotted line refers to the constant velocity interface movement $H_0 - ta^2\Sigma_e/(\zeta\alpha_m)$. The inset shows the the deviation from the constant velocity interface movement, $H - [H_0 - ta^2\Sigma_e/(\zeta\alpha_m)]$, at short times. The corresponding Pe_Σ are also shown.

Fig. 5.2. However, in this case the structural heterogeneity is also important. When $\mathrm{Pe}_U \gg 1$, the Brownian relaxation becomes ineffective, and the structural change is dominated by the moving boundary, which sweeps the particles into its vicinity and forms a growing particle front. As the particle front comes to contact with the stationary substrate, the resulting heterogeneous structure is easily jammed and quickly ends the simulation. At $\mathrm{Pe}_U = 500$, the compression on average terminates at $H = 7.3a$, well before any solid phase formation in the phase diagram. Moreover, the large variations in the terminal H at high Pe_U suggest that the jammed structures are quite different from each other, as any particle network in contact with both boundaries may force the simulation to stop.

With constant imposed normal stress Σ_e, the interface movement may be slowed down by the suspension stress build-up, allowing more time for structural relaxation. The interface stops moving when the external suspension osmotic pressure matches the normal stress, and fluctuates around an equilibrium position afterwards. Meanwhile, the suspension evolves towards the equilibrium structures at the corresponding H and ϕ in the phase diagram of Fig. 5.3 inset. In this case, the simulations are stopped manually. Unlike the interface motion with constant velocity, where a higher Pe_U corresponds to a larger terminal H, a higher Pe_Σ corresponds to a smaller terminal H as relaxation is allowed. As indicated in Eq. (5.3) and (5.4), each Pe_Σ corresponds to a continuous change of Pe_U from 0 to $\mathrm{Pe}_\Sigma/\alpha_m$.

The changes of the interface location H as functions of the dimensionless time $ta\Sigma_e/\zeta$ at different Pe_Σ are shown in Fig. 5.3. Measurements from the simulations are shown in solid lines and numerical solutions of the continuum model are shown in dashed lines. Moreover, a dash-dotted line shows the interface positions evolution if $\Sigma_m = 0$, *i.e.*, the interface moves at a constant velocity as $H = H_0 - ta^2\Sigma_e/(\alpha_m\zeta)$ because $\mathrm{Pe}_U = \mathrm{Pe}_\Sigma/\alpha_m$. At the start of the interface movement, the interface movement asymptotes to constant velocity motion due to the small suspension stress on the interface Σ_m. In this case, the condition $\mathrm{Pe}_U = \mathrm{Pe}_\Sigma/\alpha_m$ roughly holds. Continuing the compression lead to an increase in Σ_m, which slows down and eventually stops the interface movement at the equilibrium position. In Fig. 5.3, the transition to the equilibrium position is smooth for small Pe_Σ, *e.g.*, at $\mathrm{Pe}_\Sigma = 0.5$, but becomes more abrupt at higher Pe_Σ, *e.g.*, at $\mathrm{Pe}_\Sigma = 50$ a sharp corner is observed near $ta\Sigma_e/\zeta = 32$. In addition, the results from the continuum model compare well with the simulation measurements, especially at $\mathrm{Pe}_\Sigma = 0.5$. Discrepancies between the model and the simulation become more apparent at higher Pe_Σ. For example, the model underestimates the equilibrium interface position at $\mathrm{Pe}_\Sigma = 1$, 10, and 50, but overestimates at $\mathrm{Pe}_\Sigma = 2$. after $ta\Sigma_e/\zeta = 34$. From later structural observations, these differences arise from using an equation of state [Eq. (5.18)] without phase transitions in the continuum model.

The inset of Fig. 5.3 presents the difference between the interface movement and the constant velocity motion $H_0 - ta^2\Sigma_e/(\alpha_m\zeta)$ at various Pe_Σ at small t. Deviation from the constant velocity movement decreases with increasing Pe_Σ, and the difference is apparent at $ta\Sigma_e/\zeta = 0.5$ even for $\mathrm{Pe}_\Sigma = 50$. The continuum model (dashed lines) captures the simulation measurements (solid lines). At small Pe_Σ, the differences between simulation and continuum model are noticeable. However, the differences become indistinguishable at $\mathrm{Pe}_\Sigma = 50$.

Suspension microstructures

We distinguish particles in crystalline and liquid-like environment using the correlational solid identification method [37, 63] based on the bond order parameters [64]. Parameters used by Marechal et al. [37] for hard-sphere sedimentation processes are suitable for the drying processes here. Identifying whether a particle i is solid or liquid involves several steps. First, we find $N_b(i)$ neighbors within a critical distance of $r_c = 2.6a$ and compute the unnormalized bond order parameter $q^u_{l,m}(i) = N_b(i)^{-1} \sum_{j=1}^{N_b(i)} Y_{l,m}(\theta_{ij}, \phi_{ij})$, where θ_{ij} and ϕ_{ij} are the polar and azimuthal angles between particle i and its neighbor j relative to a fixed axis, and $Y_{l,m}$ is the spherical harmonic function of degree l and order m. We then normalize the bond order parameter with respect to all orders, *i.e.*, $q_{l,m}(i) = q^u_{l,m}(i)/\sqrt{\sum_{m=-l}^{l} |q^u_{l,m}(i)^2|}$. This leads to the spatial correlation $d_l(i,j) = \Re[\sum_{m=-l}^{l} q_{l,m}(i) q^*_{l,m}(j)]$ for two neighboring particles i and j, with $\Re[\cdot]$ extracting the real part of a complex number, and $*$ indicating complex conjugate. For particle i, a crystalline connection is formed with particle j if the spatial correlation $d_6(i,j) > d_c$, with $d_c = 0.7$ and symmetry index $l = 6$, and the particle has $n_{\text{con}}(i)$ crystalline connections. Finally, particle i is part of a solid structure if its crystalline connection number $n_{\text{con}}(i) > n_c$ with $n_c = 4$. We further define an overall order parameter Ξ for the suspension as the fraction of crystalline particles in the simulation cell, such that $\Xi = 1$ corresponds to an entirely crystalline structure.

Fig. 5.4 presents the overall order parameter Ξ as a function of the gap width H/a for various Péclet numbers in both interface movement modes. Combining Fig. 5.4 and the inset of Fig. 5.2 reveals the influence of the moving interface on the structural evolution of the drying process. Overall, Ξ grows with reducing H, but the details differ at high and low Péclet numbers in different interface movement modes.

Beginning with the constant interface velocity film drying process in Fig. 5.4a, with $\text{Pe}_U \ll 1$, Ξ remains close to zero for the majority of H and suddenly increases rapidly towards $\Xi = 1$. Taking $\text{Pe}_U = 0.1$ for example, Ξ suddenly grows almost vertically at $H \approx 6.5a$, corresponding to a fluid-3△ phase transition in Fig. 5.2 inset. Here, the Ξ measurement is consistent with the phase diagram prediction. Therefore, the compression is quasi-equilibrium, and the structural rearrangement is thermodynamic-driven. However, the growth in Ξ slows down significantly at $H \approx 5.8a$ after the initial jump, *i.e.*, near the 3△-3□ transition in the phase diagram. In the denser 3△ phase, the structural rearrangement takes place slowly, and is easily disrupted by the moving boundary. This leads to the slower Ξ growth and the eventual simulation termination.

When $\text{Pe}_U \gg 1$, Ξ exhibits qualitatively different behaviors with decreasing H in Fig. 5.4a. Taking the Ξ evolution at $\text{Pe}_U = 50$ for example, Ξ grows slowly at large H, in contrast to the sudden growth of Ξ at small H in the $\text{Pe}_U \ll 1$ limit. When $H \approx 13a$, far from any phase boundaries in the inset of Fig. 5.2, more than 10%

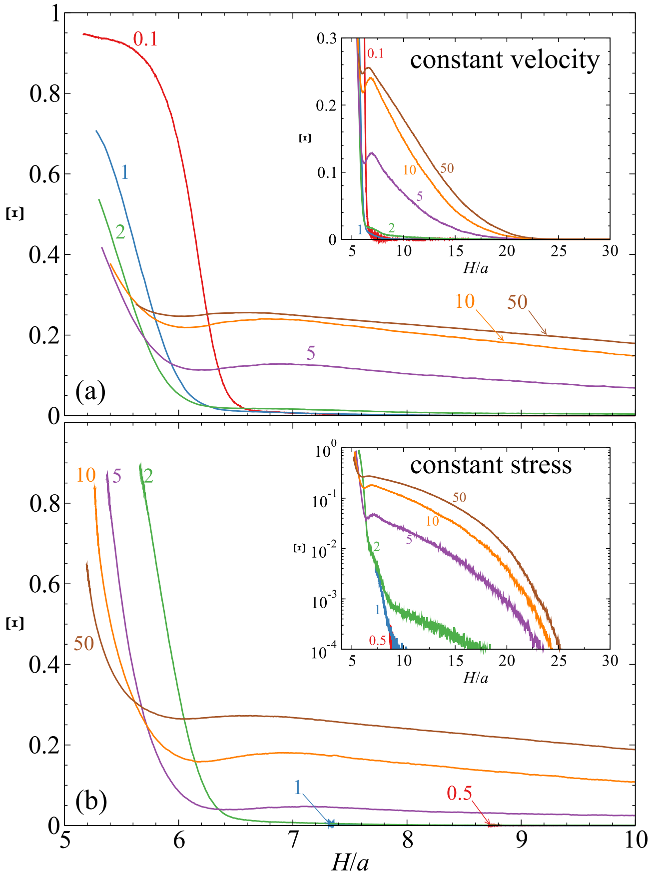

Figure 5.4: (Color online) The overall order parameter Ξ as a function of gap width H/a with (a): constant velocity interface motion with $\mathrm{Pe}_U = 0.1$, 1, 2, 5, 10, and 50, and (b) constant normal stress interface motion with $\mathrm{Pe}_\Sigma = 0.5$, 1, 2, 5, 10, and 50. The main figure and the inset show the same data with different axis scaling.

of the particles are already ordered, suggesting a heterogeneous mixture of ordered and disordered structures. More interestingly, when $H \approx 6.6a$, Ξ reaches a local maximum, decreases slightly before increasing again. We explain this observation via the growth of particle front near the moving boundary. At large H, the density next to the moving interface is high enough for crystallization, which contributes to the early increase of Ξ. As the front grows, subsequent crystallization proceeds epitaxially, *i.e.*, it uses the first layer crystals as a template for growth. Meanwhile, the particle front has to rearrange itself as it comes into contact with the stationary boundary, and this rearrangement eventually causes the "dip" in Ξ. Finally, the continued increase in Ξ suggests ordered structures are preferred at smaller H, but its formation is disrupted by the fast moving interface, leading to smaller terminal Ξ.

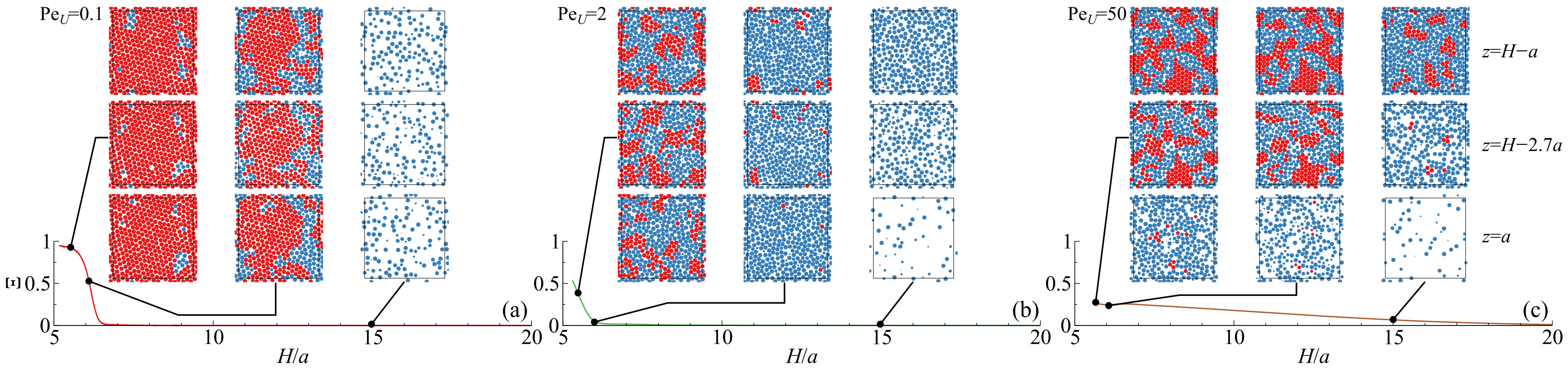

Figure 5.5: (Color online) Cut-plane views of the simulation cells at $z = H - a$, $z = H - 2.7a$, and $z = a$ at different gap locations H for (a): $\mathrm{Pe}_U = 0.1$, (b): $\mathrm{Pe}_U = 2$, and (c): $\mathrm{Pe}_U = 50$. The crystalline particles are colored red, and amorphous particles are colored blue. The corresponding evolution of Ξ as functions of H is also presented.

The evolution of Ξ in Fig. 5.4a demonstrates that the moving boundary alters the suspension structure via different mechanisms: when $\mathrm{Pe}_U \ll 1$, it induces spontaneous crystallization at small H by (almost) uniformly increasing the suspension density, and when $\mathrm{Pe}_U \gg 1$, it directly introduces localized solidification at larger H. The moving boundary also disrupts the spontaneous crystallization process when the thermodynamic time scale is comparable with the convective time scale a/U_w. This means that the least ordered structure for a given H is expected at a moderate $\mathrm{Pe}_U \sim 1$. In Fig. 5.4a, taking $H = 6a$ as an example, the minimum Ξ takes place at $\mathrm{Pe}_U = 2$, when the wall movement is too slow for localized order formation but too fast for spontaneous crystallization.

For structural evolution at constant normal stress compression in Fig. 5.4b, the Ξ evolution is qualitatively similar to the case of constant interface velocity in Fig. 5.4a. The effects of the moving interface on the suspension structures are weaker as the interface can be slowed down by the suspension pressure build-up. Here, as we manually stop the simulations shortly after the equilibrium H has been reached, the structural evolution may be incomplete, *i.e.*, the terminal Ξ in Fig. 5.4b for $\mathrm{Pe}_\Sigma > 1$ could be higher should the simulations last longer. For $\mathrm{Pe}_\Sigma = 0.5$ and 1, however, the overall Ξ is vanishingly small throughout the compression because the equilibrium position is in the liquid phase.

Fig. 5.5 shows cut-plane views of the simulation cell at, from top to bottom, $z = H-a$, $z = H - 2.7a$, and $z = a$, corresponding the particle center positions of the immediate particle layer next to the moving interface, the immediate second particle layer adjacent to a close-packed first layer, and the first layer next to the stationary boundary, respectively, at different H during the constant interface velocity film drying process. The corresponding Ξ evolution as a function of H is also presented. The particle intersections are shown as discs in the cut-plane views, with crystalline particles colored red and amorphous particles colored blue. Fig. 5.5a, 5.5b, 5.5c respectively presents the results at $\mathrm{Pe}_U = 0.1$, 2, and 50. These cut-plane views provide direct qualitative assessment of the suspension structural evolution.

The first feature revealed in Fig. 5.5 is the particle distributions during the compression. At $\mathrm{Pe}_U = 0.1$, Fig. 5.5a shows that the densities in the cut-plane views at different z-positions are approximately the same, suggesting an almost homogeneous suspension during the drying process. On the other hand, at $\mathrm{Pe}_U = 50$, Fig. 5.5c shows large density variations with respect to z. At $H = 15a$, the densities at all three cut-plane views are already quite different. At smaller H, differences between views at $z = H - a$ and $z = H - 2.7a$ becomes less apparent, but their densities are still visibly higher than those at $z = a$. With an intermediate $\mathrm{Pe}_U = 2$ in Fig. 5.5b, at $H = 15a$ the density at $z = a$ is lower than the the density near the moving interface. However, the differences are less evident when $H = 6a$ and $5.5a$.

The second feature shown in Fig. 5.5 is the crystalline structures along with the Ξ evolution. At $\mathrm{Pe}_U = 0.1$, the suspension becomes crystalline with the Ξ increase, evidenced by the red discs in Fig. 5.5a. From the cut-plane views at $H = 6a$ and $5.5a$, the crystallization process takes place uniformly across the gap. At $H = 5.5a$, almost all particles in the suspension are crystalline. The few amorphous particles are due to defects such as stacking faults. For fast interface movement at $\mathrm{Pe}_U = 50$ in Fig. 5.5c, patches of crystalline structures emerge as early as $H = 15a$ next to the moving interface. The size of the crystal patches grow with continued compression. Moreover, using the existing crystalline structures next to the moving boundary as a template, a second layer of crystalline structures also start to grow epitaxially. Before the simulation stops at $H = 5.7a$, the crystalline structures remains patchy, as the fast moving interface does not permit further structural rearrangement. The structural evolution at $\mathrm{Pe}_U = 2$ in Fig. 5.5b shows a competition between the thermodynamic-driven crystallization process at low Pe_U and the kinetic crystallization process at high Pe_U. The net result is deferred crystallization onset. At $H = 6a$, the suspension remains mostly amorphous despite nearly uniform densities across the gap. Here, Brownian motion is strong enough to redistribute particles, but too weak relative to the boundary movement to organize local ordering. Patchy crystals are only observed at $H = 5.5a$. Therefore, the structures of the colloidal film can be controlled by carefully adjusting the interface speed U_w. Crystallization at high Pe_U in Fig. 5.5c explains the recent success of fast colloidal crystal fabrication with high drying rate [27]. Moreover, the amorphous structures at moderate Pe_U may find applications in angle independent photonic materials[2].

Further characterization of the thin film structures next to the moving boundary at $z = H - a$ with the gap spacing $H = 6a$ is presented in Fig. 5.6 using the two-dimensional radial distribution function in the xy-plane, $g_{xy}(r_{xy})$, averaged over all simulations. For clarity, $g_{xy}(r_{xy})$ at $\mathrm{Pe}_U = 2$ and 50 are shifted upwards by 2 and 4, respectively. The inset of Fig. 5.6 also show the planar pair distribution function corresponding to the cut-plane views in Fig. 5.5. At $\mathrm{Pe}_U = 0.1$, the radial distribution function $g_{xy}(r_{xy})$ shows a mild double peak near $r_{xy} = 4a$, suggesting crystalline structures with relatively low density. The crystalline structure is further

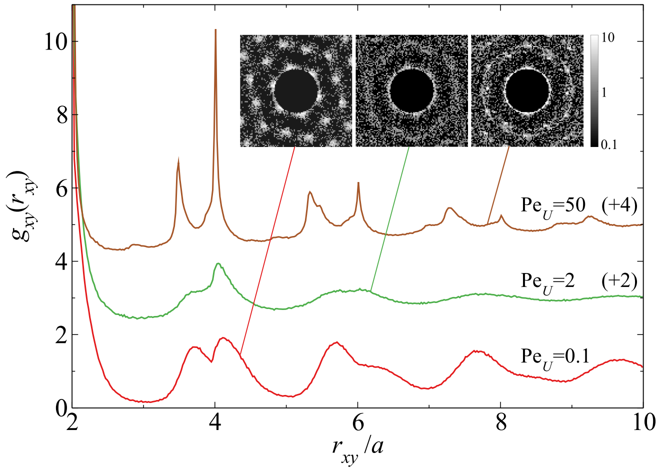

Figure 5.6: (Color online) The average planar radial distribution function in the xy-plane, $g_{xy}(r_{xy})$, measured at $z = H - a$ for $\mathrm{Pe}_U = 0.1$, 2, and 50 when the gap width $H = 6a$. The results at $\mathrm{Pe}_U = 2$ and 50 are shifted up by 2 and 4, respectively, for clarity. The insets show the 2D planar pair distribution function corresponding to the top snapshot in the middle column in Fig. 5.5a, 5.5b, and 5.5c.

confirmed by the hexagonal patterns in the corresponding pair distribution function. At $\mathrm{Pe}_U = 2$, the double peak for $g_{xy}(r_{xy})$ around $r_{xy} = 4a$ vanishes, suggesting amorphous suspension structure. The overall features in $g_{xy}(r_{xy})$ is less pronounced comparing to other Pe_U, and the pair distribution function is almost isotropic. At $\mathrm{Pe}_U = 50$, the peaks in $g_{xy}(r_{xy})$ becomes much sharper comparing to those at lower Pe_U, suggesting the particles are more densely packed. The split peaks near the second coordinate layer are at $3.5a$ and $4.0a$, closely correspond to closely packed hexagons, which show peaks at $2\sqrt{3}a$ and $4a$. The pair distribution function is a mixture of amorphous and crystalline structures, consistent with the qualitative observations in Fig. 5.5c.

The structural features for constant normal stress compression are qualitatively similar to those in Fig. 5.5 and 5.6, except for the weaker influences of the interface. The suspension is in general more ordered. For the particle layer immediately next to the moving interface, at $\mathrm{Pe}_\Sigma = 2$ and $H = 6a$, the second peak of $g_{xy}(r_{xy})$ is less pronounced and located at larger r compared to the constant velocity counterpart. Due to the similarity, these results are not presented.

Normal stress profiles

We measure the normal stress profile in the z-direction, $\Sigma_{zz}(z)$, using the method of Todd et al. [65], which, although derived for Hamiltonian systems, is also applicable for dissipative Brownian systems without hydrodynamic interactions. The stress components related to the z-direction at position z' is

$$\langle \Sigma_{z\alpha}(z') \rangle = -\langle n(z') \rangle k_{\mathrm{B}} T \delta_{z\alpha} - \frac{1}{2A} \left\langle \sum_{i=1}^{N} f_{i\alpha}^{\mathrm{P}} \mathrm{sgn}(z_i - z') \right\rangle, \ \alpha \in \{x, y, z\}, \quad (5.19)$$

where $\langle \cdot \rangle$ denotes an ensemble average, $n(z')$ is the local particle number density, $A = L^2$ is the xy area of the simulation cell, and $F_{i\alpha}^{\mathrm{P}}$ is the *interparticle* force in the α direction of particle i. Eq. (5.19) suggests that the local stress is intimately related to the total force across the plane. The first term on the right hand side of Eq. (5.19) is simplified from the original formulation for the isothermal Brownian suspensions. Note that the *interparticle* force $\boldsymbol{f}_i^{\mathrm{P}}$ for particle i excludes the forces from the confining boundaries, $\boldsymbol{f}_i^{\mathrm{W}}$. Since Eq. (5.19) involves all particles in the simulation box, it provides better local stress resolution comparing to spatial binning, which is susceptible to large noises at small bin widths [65]. The EMPF algorithm also eliminates the ambiguous stress definition from multiple overlaps.

To avoid inaccuracies from contact density measurement next to the wall—an inherent drawback of the time discretization algorithms—the contact stresses on the moving interface, Σ_m, and on the stationary substrate, Σ_s, are directly computed as

$$\Sigma_m = -\frac{1}{2A\Delta t} \sum_{r=1}^{l^+} \lambda_r^+ \quad \text{and} \quad \Sigma_s = -\frac{1}{2A\Delta t} \sum_{t=1}^{l^-} \lambda_t^-, \quad (5.20)$$

where λ_r^+ and λ_t^- are the wall confinement Lagrange multiplier defined in the appendix, and their values divided by Δt are twice the force exerted by the wall on particle r or t.

Fig. 5.7 and 5.8 present the suspension normal stress profiles $\Sigma_{zz}/(n_0 k_{\mathrm{B}} T)$, with $n_0 = \frac{3}{4}\phi_0/(\pi a^3)$, along with the moving interface stresses at different Péclet numbers for, respectively, the constant velocity and the constant normal stress drying processes. In both figures, the simulation measurements are presented on the left column while the continuum model results on the right. For constant velocity interface movement in Fig. 5.7, Σ_{zz} on the moving boundary eventually diverges, and the stress difference between the two boundaries increases with Pe_U. On the other hand, for drying process with constant imposed normal stress in Fig. 5.8, Σ_{zz} does not diverge, and near the equilibrium wall position, the stress profile eventually becomes

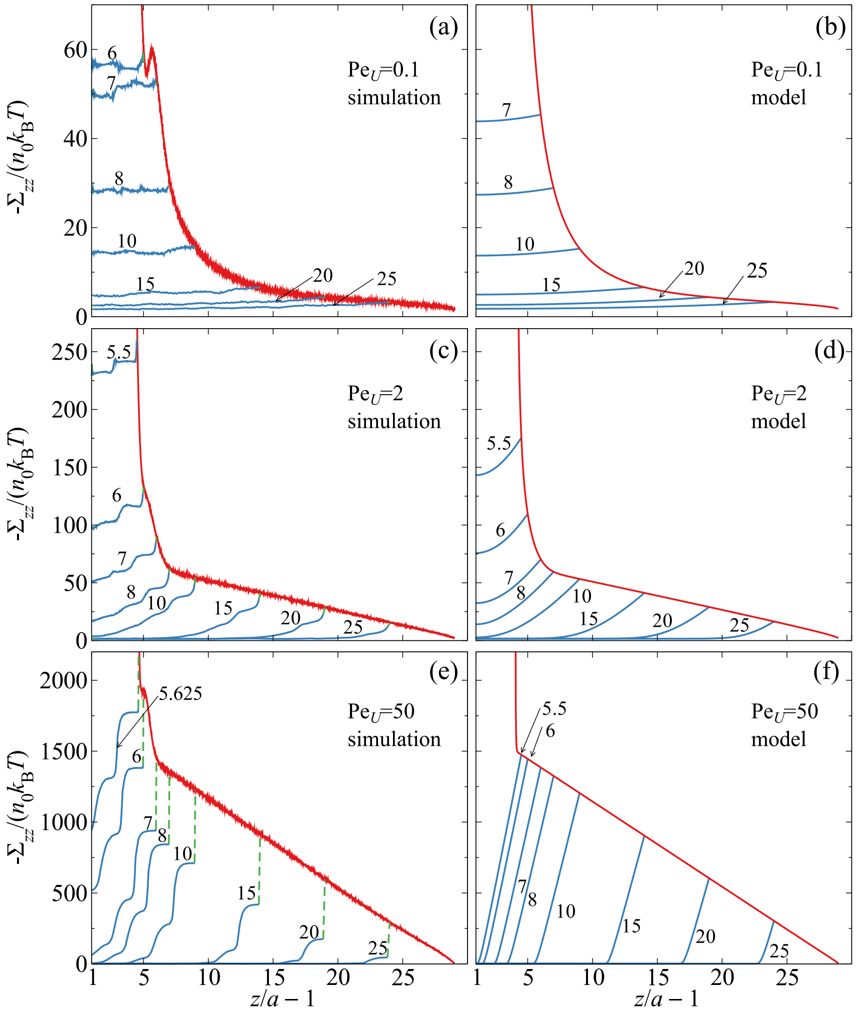

Figure 5.7: (Color online) The normal stress profiles $\Sigma_{zz}/(n_0k_BT)$ in drying processes with constant velocity interface movement at (a), (b): $\mathrm{Pe}_U = 0.1$, (c), (d): $\mathrm{Pe}_U = 2$, and (e), (f): $\mathrm{Pe}_U = 50$. Simulation measurements are shown in (a), (c), and (e), and continuum model results are shown in (b), (d), and (f). To reduce noise, simulation stress measurements are averaged over $0.01a$. The normal stresses on the moving interface are shown in red, and the stress profiles at the denoted H/a are shown in blue. Near the boundaries, the contact stress and the suspension stress are connected by green dashed lines, visible only at high Pe_U due to stress concentration.

uniform across the gap, and suspension stress on the boundary eventually matches the imposed stress Σ_e.

Let us begin with the normal stress measurements in Fig. 5.7a, 5.7c, 5.7e for constant velocity interface movement. For $\mathrm{Pe}_U \ll 1$, the stress distribution across the gap reflects Brownian motion dominance. For example, at $\mathrm{Pe}_U = 0.1$ (Fig. 5.7a), the

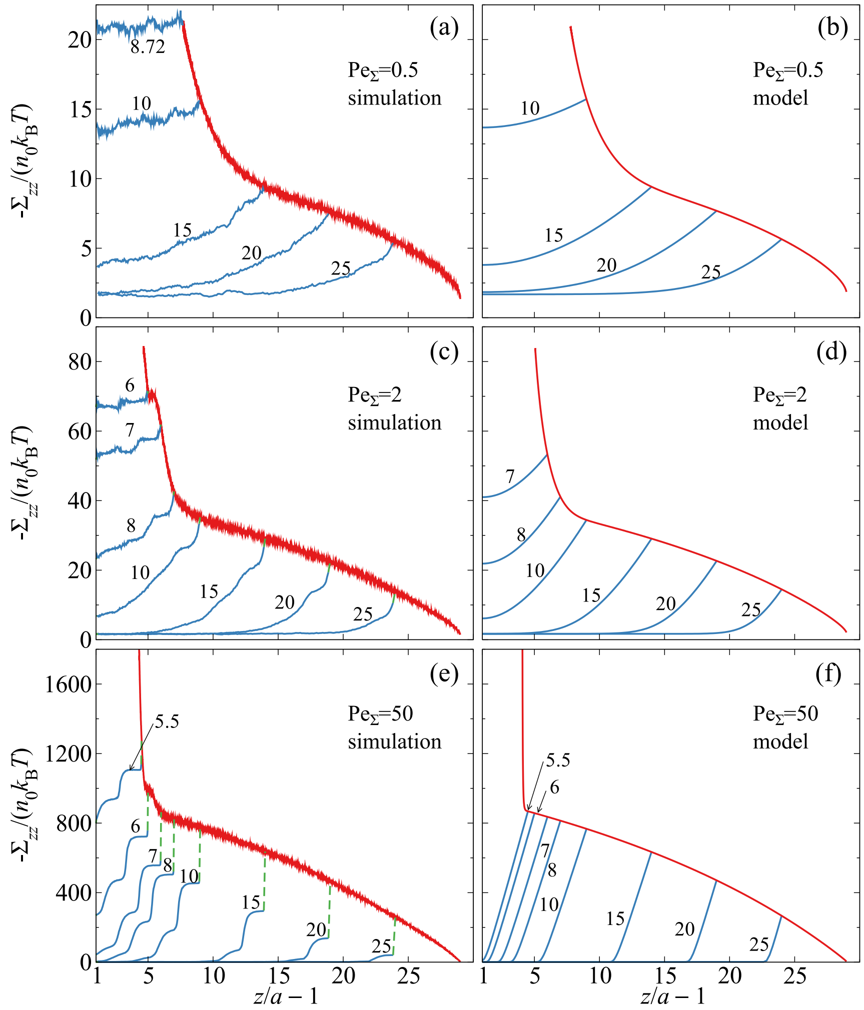

Figure 5.8: (Color online) The normal stress profiles $\Sigma_{zz}/(n_0 k_\mathrm{B}T)$ in drying processes with constant normal stress interface movement at (a), (b): $\mathrm{Pe}_\Sigma = 0.5$, (c), (d): $\mathrm{Pe}_\Sigma = 2$, and (e), (f): $\mathrm{Pe}_\Sigma = 50$. Simulation measurements are shown in (a), (c), and (e), and continuum model results are shown in (b), (d), and (f). Other arrangements are identical to Fig. 5.7.

stresses on the moving boundary increase with decreasing H, except a reduction between $H \approx 6.6a$ and $6.1a$. This reduction coincides with the abrupt increase of Ξ in Fig. 5.4a due to crystallization to the $3\triangle$ phase in the phase diagram. Therefore, the stress is reduced by the thermodynamic structural rearrangement. From the almost uniform stress distribution across the gap, the stress differences between the stationary and the moving boundaries are small due to strong Brownian motion. In addition, the stress profile becomes more inhomogeneous near the structural transition, *i.e.*, at $H = 7a$. Here, the higher stress on the moving boundary suggests the higher local density, which initiates the spontaneous crystallization.

At $\mathrm{Pe}_U \gg 1$, the structural heterogeneity leads to strong stress heterogeneity. On the moving boundary, the normal stress evolution with reducing H can be divided into four stages. Using the case of $\mathrm{Pe}_U = 50$ in Fig. 5.7e as an example, they are: (*i*) linear normal stress increase from the beginning to $H \approx 7a$. This reflects the normal stress required to carry the growing particle front at a constant velocity. The linearity implies linear particle front growth as the initial particle distribution is uniform. (*ii*) Abrupt stress increase over a short distance between $H \approx 7a$ and $6a$. The particle front begins to be in contact with the stationary boundary and is compressed, giving rise to a local Ξ maximum in Fig. 5.4a. (*iii*) Slower stress increase near $H/a = 6$. This slower stress growth is consistent with the onset of Ξ increase after the "dip" in Fig. 5.4a, *i.e.*, the tendency for crystallization in a dense and heterogeneous structure is strong enough to slow down the stress increase. (*iv*) Continued stress increase until simulation stops from compressing a jammed structure. Clearly, the stress on the moving interface is consistent with the suspension structural evolution. For moderate Pe_U, *e.g.*, $\mathrm{Pe}_U = 2$ in Fig. 5.7c, stage (*iii*) disappears completely together with the Ξ "dip" in Fig. 5.4a due to a lack of order in the suspension. Moreover, the stress distribution across the gap at large Pe_U is more complicated. Near the moving interface, the stresses measured in the suspensions from Eq. (5.19) are different from the stress measured on the interface via Eq. (5.20), suggesting boundary-layer-like stress variation in this region. Away from the boundaries, the stress exhibits a step-like profile, and remains inhomogeneous during the drying process. The stress profiles here are consistent with the structural heterogeneity.

The normal stress profiles for interface movement with constant imposed normal stress, shown in Fig. 5.8a, 5.8c, and 5.8e, share many similarities with those of constant velocity compression. As indicated earlier, in this compression mode the normal stress no longer diverges, and eventually matches the imposed stress. In the $\mathrm{Pe}_\Sigma \ll 1$ limit, qualitative features of the stress profile remain unchanged, but in the $\mathrm{Pe}_\Sigma \gg 1$ limit, the slowdown of the moving interface changes the linear $\Sigma_{zz}/(n_0 k_\mathrm{B} T)$ growth in stage (*i*) of the $\mathrm{Pe}_U \gg 1$ case to a curve, *e.g.*, the case of $\mathrm{Pe}_\Sigma = 50$ in Fig. 5.8e. Other stages of stress development discussed earlier remain similar. Stress concentration in the stress boundary layer remains at the beginning of the compression for $\mathrm{Pe}_\Sigma \gg 1$. However, with decreasing H, the stress boundary layer vanishes and the stress difference between the two boundaries diminishes, again due to relaxation from the slowing moving interface.

In Fig. 5.7 and 5.8, the normal stress computed from the continuum model, $\Sigma_{zz}(z) =$

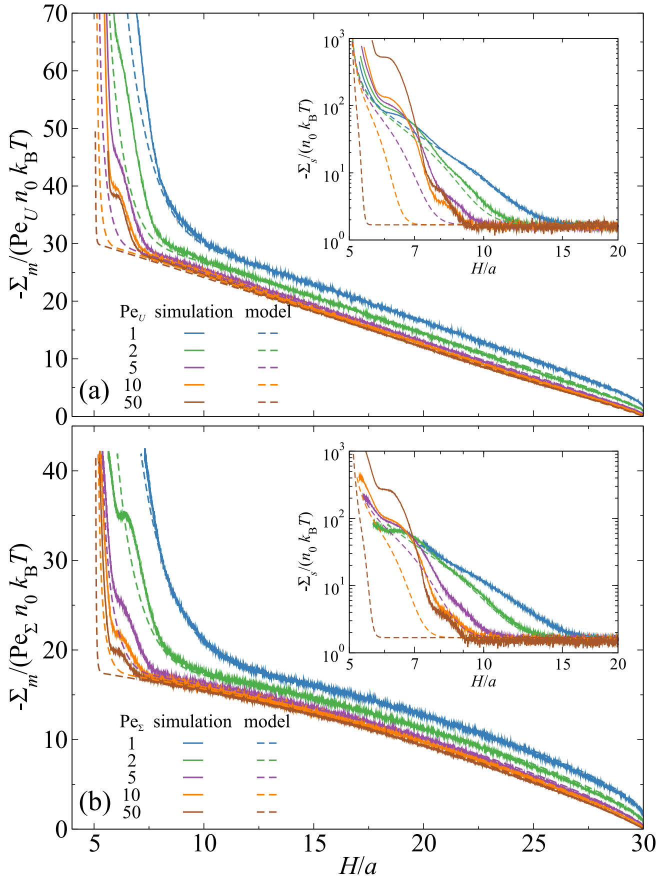

Figure 5.9: (Color online) The scaled suspension stress on the moving interface as functions of the gap width H/a for (a): $\Sigma_m/(\mathrm{Pe}_U n_0 k_\mathrm{B} T)$ for drying with an interface at constant velocity at (from right to left) $\mathrm{Pe}_U = 1$, 2, 5, 10, and 50 and (b): $\Sigma_m/(\mathrm{Pe}_\Sigma n_0 k_\mathrm{B} T)$ for drying with an interface subject to constant normal stress at (from right to left) $\mathrm{Pe}_\Sigma = 1$, 2, 5, 10, and 50. The insets show the stress on the stationary boundary $\Sigma_s/(n_0 k_\mathrm{B} T)$ as functions of gap spacing for the same Pe_U or Pe_Σ. The simulations results are shown in solid lines and model computations are shown in dashed lines.

$\frac{3}{4} k_\mathrm{B} T \phi Z(\phi)/(\pi a^3)$, not only captures the qualitative, but also some quantitative aspects of the simulation results, particularly the normal stresses evolution on the boundaries. The continuum model agrees excellently with the simulation until the onset of solidification in the simulation when $\mathrm{Pe}_U \ll 1$, *i.e.*, comparing Fig. 5.7a and 5.7b at $\mathrm{Pe}_U = 0.1$, the model agrees with the simulations up to $H \approx 7a$. Without crystallization, *e.g.*, in Fig. 5.8a and 5.8b at $\mathrm{Pe}_\Sigma = 0.5$ with constant normal stress interface movement, the agreement between the model and the simulation is present over the entire drying process. At larger Pe_U and Pe_Σ, the model can predict the boundary normal stresses in both interface movement modes until significant structural rearrangement takes place in the simulation. However, the continuum model is unable to capture the complex, step-like, stress profiles. For example, at $\mathrm{Pe}_U = 50$ and $\mathrm{Pe}_\Sigma = 50$, the model can only capture the moving wall normal stress during stage (*i*) and (*ii*) of the stress evolution. Considering how simple the parameter-free model is, *i.e.*, ignoring the structural transitions and non-local effects, this agreement is remarkable.

Finally, Fig. 5.9 presents the moving stress evolution during the compression scaled with the corresponding Péclet number, $-\Sigma_m/(\mathrm{Pe}_U n_0 k_\mathrm{B} T)$ in Fig. 5.9a for $\mathrm{Pe}_U \geq 1$ and $-\Sigma_m/(\mathrm{Pe}_\Sigma n_0 k_\mathrm{B} T)$ in Fig. 5.9b for $\mathrm{Pe}_\Sigma \geq 1$. The stress evolution at different Péclet number collapses onto a master curve for different interface movement profile during stage (*i*) of the stress evolution in the high Péclet number limit. The collapse suggests that with $\mathrm{Pe}_U \gg 1$ or $\mathrm{Pe}_\Sigma \gg 1$, the stress on the moving interface is dominated by convection: at constant velocity interface movement, the faster the moving interface pushes the growing particle front, the larger the stress required; and with constant imposed normal stress, the growing particle front slows down the moving interface in a way that is proportional to the imposed stress. Furthermore, all data in Fig. 5.9b share the same maximum $\Sigma_m/(\mathrm{Pe}_\Sigma n_0 k_\mathrm{B} T)$, because $\Sigma_{zz}/(\mathrm{Pe}_\Sigma n_0 k_\mathrm{B} T) = (\Sigma_{zz}/\Sigma_e)(\frac{4}{3}\pi/\phi_0)$ and at equilibrium $\Sigma_{zz} = \Sigma_e$. Therefore, the scaled stress maximum is 41.9 for $\phi_0 = 0.1$, consistent with Fig. 5.9b. Here, the continuum model in dashed line agrees excellently with the simulation when $H > 7a$. At smaller gap width, structural rearrangement drives the model prediction away from the simulation data. The discrepancy is especially apparent at higher Pe_U or Pe_Σ.

The inset of Fig. 5.9 presents the stress on the stationary boundary, $\Sigma_s/(n_0 k_\mathrm{B} T)$, as functions of the gap spacing H in the corresponding compression mode at different Péclet numbers. The $\Sigma_s/(n_0 k_\mathrm{B} T)$ behaviors are similar between different interface movement modes, but do not collapse with the Péclet numbers like the stresses on the moving interface. For $\mathrm{Pe}_U \geq 1$ and $\mathrm{Pe}_\Sigma \geq 1$, the growth of $\Sigma_s/(n_0 k_\mathrm{B} T)$ is deferred, *e.g.*, Σ_s only begins to grow at $H \approx 15a$ with $\mathrm{Pe}_U = 1$ and at $H \approx 10a$ with $\mathrm{Pe}_U = 10$ in Fig. 5.9a. Prior to the growth, the stationary boundary stress remains a constant. The growth of $\Sigma_s/(n_0 k_\mathrm{B} T)$ takes place at smaller H with increasing Pe_U or Pe_Σ. This is because, physically, Σ_s only begins to change when the particle front becomes in contact with the stationary boundary. The continuum model captures the behaviors of Σ_s at low Pe_U and Pe_Σ, but underestimates the gap width where Σ_s

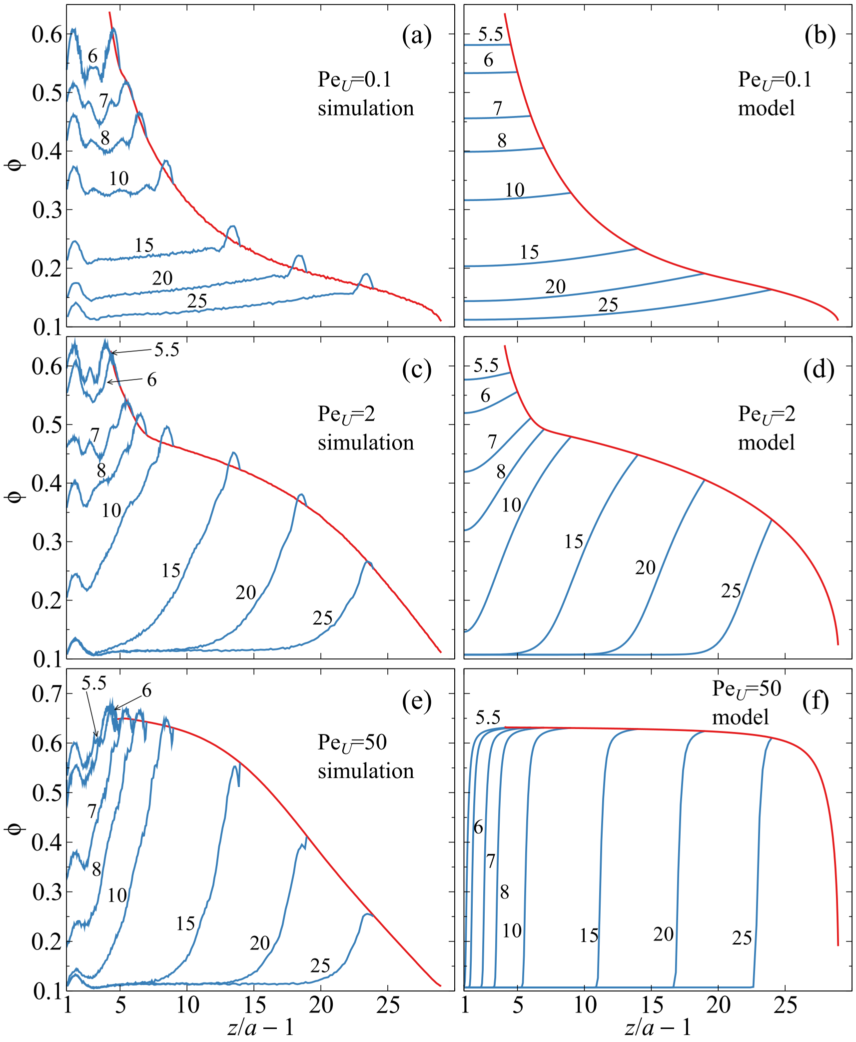

Figure 5.10: (Color online) Local volume fraction profile $\phi(z)$ in drying process with constant velocity interface movement at (a), (b): $\mathrm{Pe}_U = 0.1$, (c), (d): $\mathrm{Pe}_U = 2$, and (e), (f): $\mathrm{Pe}_U = 50$. Simulation measurements are shown in (a), (c), and (e), and continuum model results are shown in (b), (d), and (f). The local volume fractions next to the moving interface are shown in red, and the volume fraction profiles at the denoted H/a are shown in blue.

begins to grow, as the continuum model cannot resolve the structural evolution of the particle front.

Volume fraction profiles

Measuring the local volume fraction ϕ within the gap provides a direct comparison between the simulation and the continuum model. Unlike the number density n which can be sensitive to the measurement resolution near the fast moving interface, the volume fraction is always bounded. The local volume fractions are computed by partitioning the simulation cell using Voronoi tessellation [66] with periodic boundary conditions in the x- and y-directions. In the z-direction, the part of the simulation cell that is inaccessible to particles is omitted, *i.e.*, the tessellation is limited between $z = a$ and $z = H - a$. For each particle i, the ratio of the particle volume $V_{p,i}$ to the tessellation cell volume $V_{c,i}$ defines the local volume fraction of the particle $\phi_i = V_{p,i}/V_{c,i}$. The volume fraction profile $\phi(z)$ is obtained by sorting and averaging ϕ_i based on their z-position. Comparing to other coarse-grained approaches [39], this is parameter-free and provides satisfactory spatial resolution.

Fig. 5.10 shows the simulation and the continuum model local volume fraction $\phi(z)$ across the gap at various H during the constant interface velocity drying process at $\mathrm{Pe}_U = 0.1$ (Fig. 5.10a, 5.10b), $\mathrm{Pe}_U = 2$ (Fig. 5.10c, 5.10d), and $\mathrm{Pe}_U = 50$ (Fig. 5.10e, 5.10f). The local volume fractions next to the moving interface are also shown. The simulation measurements are presented in the left and the computation from the continuum model on the right. Results from constant imposed normal stress are almost identical and therefore are not shown. That the almost identical ϕ profiles produce distinct stress development in two interface movement modes suggests the sensitivity of the local stress $\Sigma_{zz}(z)$ to the local volume fraction $\phi(z)$.

The measured local volume fraction is bounded by the Voronoi tessellation. For example, in Fig. 5.10a at $\mathrm{Pe}_U = 0.1$, the maximum ϕ from the simulations is ~ 0.65 despite extensive solidification, significantly lower than the bulk maximum $\phi \sim 0.74$ for fcc solids. Fluctuations in the ϕ measurements near the boundaries are due to measurement protocol, and the fluctuations at small H arises from crystallization. With $\mathrm{Pe}_U = 0.1$ in Fig. 5.10a, the ϕ profile is almost linear across the gap for $H \geq 15a$, and the ϕ difference between the moving interface and the stationary boundary is small. Therefore, the particle flux is almost constant across the gap due to abundant thermal fluctuations. At smaller H, the ϕ distribution becomes more symmetric due to crystallization. For $\mathrm{Pe}_U = 50$ in Fig. 5.10e, the ϕ profile shows more variations across the gap. The ϕ profile for $H \geq 15a$ clearly indicates the formation of a particle front with an advancing interface. When $H \approx 10a$, the particle front is in contact with the stationary boundary and begins to rearrange. The rearrangement is localized, causing significant ϕ increase near the stationary boundary, but not much change near the moving interface. The larger ϕ fluctuations near $H = 6a$ are due to crystallization. Qualitatively, the ϕ profiles at $\mathrm{Pe}_U = 2$ and $\mathrm{Pe}_U = 50$ from the simulations are similar.

The continuum model accurately predicts the ϕ profile at $\mathrm{Pe}_U \ll 1$ with $H > 7a$, but fails to capture the ϕ fluctuations at small H from the crystallization process. At higher Pe_U, the continuum model disagrees with the simulation measurements on the changes in ϕ next to the moving interface. This is especially pronounced at $\mathrm{Pe}_U = 50$: the model predicts that ϕ near the moving interface becomes almost constant when $H < 20a$. However, the corresponding simulation measurements show a much slower ϕ growth. Moreover, the simulation shows a more diffusive particle front near the moving wall, in contrast to the sharp interface predicted by the model. This "diffusive" front, however, is not due to the Brownian motion, but the finite particle size—an aspect not captured by the model.

Improving the continuum model is challenging. For example, incorporating the effects of convection on the particle mobility, *i.e.*, changing d_0 in Eq. (5.13) and (5.15) to collective diffusivity $d_c(\phi) = (1 + \mathrm{Pe}_U b)$ or $d_c(\phi) = (1 + \mathrm{Pe}_U b\phi)$—with b a fitting parameter—did not yield qualitative improvement. It should be recalled that the particle size does not enter the continuum model and therefore non-local, particle-scale effects similar to those proposed by Kamrin and Koval [51] for particle mobility may be helpful. Nonetheless, the existing continuum model successfully captures the ϕ evolution at small Péclet numbers and large H in both interface movement modes. The success of the model may be that the equation of state, Eq. (5.18), accurately captures the behaviors of the amorphous suspensions under confinement.

5.4 Concluding Remarks

We presented a simulation and modeling investigation on the colloidal film drying process with the interface moving at constant velocity or subject to constant imposed stresses. For the simulations, we developed a new EMPF algorithm to address the unique challenges in the drying process. The simulation results are compared with a continuum model, also developed in this work, to understand their validity.

At low Péclet numbers, the drying dynamics are dominated by Brownian motion up to small gap widths. Changes in suspension structures and stresses can be succinctly summarized by constructing an operating curve on the confined suspension phase diagram [30]. At high Péclet numbers, a growing particle front emerges next to the moving interface, which leads to structural heterogeneity. As a result, the stress profiles exhibit a stress boundary layer next to the moving interface, and step like stress profiles within the gap. Our simulations show that different suspension structures from amorphous to crystalline can be obtained by adjusting interface motion. Interestingly, for a given H, the most amorphous structures are found at moderate Péclet numbers as the moving interface promotes localized crystallization and disrupts spontaneous phase transition. With constant imposed normal stress, the influence of the moving interface is weaker as the interface velocity can be reduced. The simple continuum model successfully captures the dynamics of the suspension at low Péclet numbers, but shows limited success at high Péclet numbers. The model predicts the interface stress and position in both compression modes, but cannot describe the stress and volume fraction profiles, suggesting the importance of phase transitions and non-local effects in the model construction.

This work provides an in-depth structural and mechanical characterization of the colloidal film drying process. It also sheds light on the non-equilibrium, boundary-driven transport processes of confined systems in general. It shows that film structure may be controlled by changing the interface movement, demonstrating the unexpectedly important role of convective transport on the film formation process and the colloidal self-assembly processes in general. The comparison between the continuum model and the simulation also show the need for new model developments that properly account for the convection effects.

A possible extension of this work is the incorporation of hydrodynamic interactions. Hydrodynamics profoundly affect the dynamics and transport of the confined colloidal suspensions [12, 15]. The influences of hydrodynamic interactions on the drying process are unknown, including the structural consequences of the reduced particle mobility and the long-range correlated particle motion. Their effects can only be assessed via detailed hydrodynamic simulations.

5.A Cost functions for confined systems

Additional cost functions to account for the interactions between the boundary and the clusters are necessary to use the EMPF algorithm for the film drying process. We assume that the boundaries are reflective in the z-direction and perfectly slip in the x- and y-directions. With constant interface velocity, the wall motion is deterministic. However, when the interface is subject to constant normal stress, the interface position also changes by interacting with the overlapping particles.

For the deterministic interface movement, the boundaries impose new geometric constraints, and remove the force-free constraints in the z-direction. Given an n-particle cluster with m overlapping particle pairs, l_+ and l_- particles overlapped with the boundary at $z = H$ and $z = 0$, respectively, the cost function for particles with radii a is

$$\begin{aligned} f_c^{fw}(\boldsymbol{y}) = &\sum_{i=1}^{n} \epsilon_i + \sum_{s=1}^{m} \lambda_s^p [\|(\boldsymbol{x}_p + \Delta \boldsymbol{x}_p^{\mathrm{P}}) - (\boldsymbol{x}_q + \Delta \boldsymbol{x}_q^{\mathrm{P}})\|^2 - 4a^2] \\ &+ \sum_{r=1}^{l_+} \lambda_r^+ [(H - a) - (z_r + \Delta z_r^{\mathrm{P}})] + \sum_{t=1}^{l_-} \lambda_t^- [(z_t + \Delta z_t^{\mathrm{P}}) - a] \\ &+ \lambda_x^f \sum_{i=1}^{n} f_{i,x}^{\mathrm{P}} + \lambda_y^f \sum_{i=1}^{n} f_{i,y}^{\mathrm{P}}, \end{aligned} \tag{5.21}$$

where z_r and Δz_r^{P} are respectively the z-position and displacement of particle r overlapped with the boundary at $z = H$, and z_t and Δz_t^{P} are similar quantities with the boundary at $z = 0$, and the unknown vector is

$$\boldsymbol{y} = (\{\Delta \boldsymbol{x}_i^{\mathrm{P}}\}_n, \{\lambda_s^p\}_m, \{\lambda_r^+\}_{l_+}, \{\lambda_t^-\}_{l_-}, \lambda_x^f, \lambda_y^f). \tag{5.22}$$

When the interface is subject to a constant normal stress, its position change due to particle overlaps has to be solved as part of the problem. From Eq. (5.4), the force required to move the boundary a distance ΔH^{P} in z-direction is $f_m^{\mathrm{P}} = \zeta \alpha_m (L^2/a^2)(\Delta H^{\mathrm{P}}/\Delta t)$, and the energy associated with such motion is $\epsilon_m = f_m^{\mathrm{P}} \Delta H^{\mathrm{P}}$. If the cluster only overlaps with the moving boundary at $z = H$, the wall is treated as a large particle, and the cost function is augmented from Eq. (5.11):

$$\begin{aligned} f_c^{mw}(\boldsymbol{y}) = &\sum_{i=1}^{n} \epsilon_i + \epsilon_m + \sum_{s=1}^{m} \lambda_s^p [\|(\boldsymbol{x}_p + \Delta \boldsymbol{x}_p^{\mathrm{P}}) - (\boldsymbol{x}_q + \Delta \boldsymbol{x}_q^{\mathrm{P}})\|^2 - 4a^2] \\ &+ \sum_{r=1}^{l_+} \lambda_r^+ [(H + \Delta H^{\mathrm{P}} - a) - (z_r + \Delta z_r^{\mathrm{P}})] \\ &+ \boldsymbol{\lambda}^f \cdot (\sum_{i=1}^{n} \boldsymbol{f}_i^{\mathrm{P}} + f_m^{\mathrm{P}} \mathbf{1}_z), \end{aligned} \tag{5.23}$$

where $\mathbf{1}_z$ is the z-direction unit vector. In addition, the cluster may overlap with both boundaries, and the cost function is augmented from Eq. (5.21) as,

$$\begin{aligned} f_c^{tw}(\boldsymbol{y}) = &\sum_{i=1}^{n} \epsilon_i + \epsilon_m + \sum_{s=1}^{m} \lambda_s^p [\|(\boldsymbol{x}_p + \Delta \boldsymbol{x}_p^{\mathrm{P}}) - (\boldsymbol{x}_q + \Delta \boldsymbol{x}_q^{\mathrm{P}})\|^2 - 4a^2] \\ &+ \sum_{r=1}^{l_+} \lambda_r^+ [(H + \Delta H^{\mathrm{P}} - a) - (z_r + \Delta z_r^{\mathrm{P}})] \\ &+ \sum_{t=1}^{l_-} \lambda_t^- [(z_t + \Delta z_t^{\mathrm{P}}) - a] + \lambda_x^f \sum_{i=1}^{n} f_{i,x}^{\mathrm{P}} + \lambda_y^f \sum_{i=1}^{n} f_{i,y}^{\mathrm{P}}. \end{aligned} \tag{5.24}$$

The set of cost functions in Eq. (5.11), (5.21), (5.23) and (5.24) covers all possible scenarios of interface movement in this work.

5.B Solving the continuum model and mapping to simulations

The moving boundary problems in Eq. (5.13) and (5.15) and their auxiliary equations are transformed to a fixed domain of $0 \leq \xi \leq 1$ through the coordinate transformation $\xi(t) = z/L(t)$ [67]. Since particle size does not explicitly appear in the model, it is more convenient to scale the length with the initial gap width L_0. For constant velocity interface movement, we introduce a new dimensionless time $\tau = tU_w/L_0$ and a wall velocity Péclet number $\mathrm{Pe_{WU}} = U_w L_0/D_0 = \mathrm{Pe}_U(L_0/a)$, which leads to

$$\frac{\partial \phi}{\partial \tau} = \frac{1}{\mathrm{Pe_{WU}}(1-\tau)^2} \frac{\partial}{\partial \xi} \left\{ \frac{\mathrm{d}}{\mathrm{d}\phi}[\phi Z(\phi)] \frac{\partial \phi}{\partial \xi} \right\} - \frac{\xi}{1-\tau} \frac{\partial \phi}{\partial \xi} \tag{5.25}$$

with boundary conditions

$$\frac{\partial \phi}{\partial \xi} = 0 \text{ at } \xi = 0, \tag{5.26}$$

$$\frac{\mathrm{d}}{\mathrm{d}\phi}[\phi Z(\phi)] \frac{\partial \phi}{\partial \xi} - \mathrm{Pe_{WU}}(1-\tau)\phi = 0 \text{ at } \xi = 1. \tag{5.27}$$

For constant normal stress interface movement, we define $\tau = (\zeta/\Sigma_e)(L_0/a^2)$, and the wall stress Péclet number $\mathrm{Pe_{W\Sigma}} = a^2 L_0 \Sigma_e/(k_\mathrm{B}T) = \mathrm{Pe}_\Sigma(L_0/a)$. With $\bar{L} = L(t)/L_0$, we have

$$\frac{\partial \phi}{\partial \tau} = \frac{1}{\mathrm{Pe_{W\Sigma}}} \frac{1}{\bar{L}^2} \left[\frac{\mathrm{d}^2 f}{\mathrm{d}\phi^2} \left(\frac{\partial \phi}{\partial \xi} \right)^2 + \frac{\mathrm{d}f}{\mathrm{d}\phi} \frac{\partial^2 \phi}{\partial \xi^2} \right] + \frac{\xi}{\bar{L}\alpha_m} \frac{\partial \phi}{\partial \xi}(-1 + \beta f), \tag{5.28}$$

with boundary conditions

$$\frac{\partial \phi}{\partial \xi} = 0 \text{ at } \xi = 0, \tag{5.29}$$

$$\frac{1}{\bar{L}} \frac{\mathrm{d}f}{\mathrm{d}\phi} \frac{\partial \phi}{\partial \xi} + \frac{\phi \mathrm{Pe_{W\Sigma}}}{\alpha_m}(-1 + \beta f) = 0 \text{ at } \xi = 1, \tag{5.30}$$

and the wall motion auxiliary equation

$$\frac{\mathrm{d}\bar{L}}{\mathrm{d}\tau} = \frac{-1 + \beta f}{\alpha_m}, \tag{5.31}$$

where $f = \phi Z(\phi)$, and $\beta = 3/(4\pi)(L_0/a)\mathrm{Pe_{W\Sigma}^{-1}}$. These non-linear partial differential equations can be converted to a set of ordinary differential equations by spatial discretization and solved numerically.

A subtlety for comparing the simulations with the continuum models is that in the simulations the confining boundaries reduce the particle accessible volume. For a simulation starting with H_0 and ϕ_0, the corresponding continuum model has an initial gap width $L_0 = H_0 - 2a$ and a starting volume fraction $\phi_s = \phi_0 H_0/(H_0 - 2a)$. The wall position $L(t)$ in the model corresponds to $H(t) = L(t)H_0/(H_0 - 2a)$ in the simulations. Furthermore, when comparing the stress and volume fraction profiles, the simulation position z_s with $H(t)$ and the model position z_m with $L(t)$ are related as

$$\frac{z_s - a}{H(t) - 2a} = \frac{z_m}{L(t)}. \tag{5.32}$$

References

[1] S.-H. Kim, S. Y. Lee, S.-M. Yang, and G.-R. Yi, “Self-assembled colloidal structures for photonics”, NPG Asia Mater. **3**, 25 (2011).

[2] I. Lee, D. Kim, J. Kal, H. Baek, D. Kwak, D. Go, E. Kim, C. Kang, J. Chung, Y. Jang, S. Ji, J. Joo, and Y. Kang, “Quasi-amorphous colloidal structures for electrically tunable full-color photonic pixels with angle-independency”, Adv. Mater. **22**, 4973 (2010).

[3] J. J. Guo and J. A. Lewis, “Aggregation effects on the compressive flow properties and drying behavior of colloidal silica suspensions”, J. Am. Ceram. Soc **89**, 2345 (1999).

[4] D. M. Holms, F. Tegeler, and W. J. Clegg, “Stresses and strains in colloidal films during lateral drying”, J. Eur. Ceram. Soc. **28**, 1381 (2008).

[5] J. Kim, K. Cho, S. Ryu, S. Y. Kim, and B. M. Weon, “Crack formation and prevention in colloidal drops”, Sci. Rep. **5**, 13166 (2015).

[6] J. L. Keddie, “Film formation of latex”, Mater. Sci. Eng. R-Rep. **21**, 101 (1997).

[7] D. D. Brewer, T. Shibuta, L. Francis, S. Kumar, and M. Tsapatsis, “Coating process regimes in particulate film production by forced-convection-assisted drag-out”, Langmuir **27**, 11660 (2011).

[8] Y. K. Koh, C. H. Yip, Y.-M. Chiang, and C. C. Wong, “Kinetic stages of single-component colloidal crystallization”, Langmuir **24**, 5245 (2008).

[9] A. F. Routh, “Drying of thin colloidal films”, Rep. Prog. Phys. **76**, 046603 (2013).

[10] W. B. Russel, D. A. Saville, and W. R. Schowalter, *Colloidal dispersions* (Cambridge University Press, 1991).

[11] J. K. G. Dhont, *An introduction to dynamics of colloids* (Elsevier, Amsterdam, 1996).

[12] J. W. Swan and J. F. Brady, “The hydrodynamics of confined dispersions”, J. Fluid Mech. **687**, 254 (2011).

[13] A. Q. Shen and P. Cheung, “The freedom of confinement in complex fluids”, Phys. Today **63**, 30 (2010).

[14] A. W. C. Lau and T. C. Lubensky, “State-dependent diffusion: thermodynamic consistency and its path integral formulation”, Phys. Rev. E **76**, 011123 (2007).

[15] H. Diamant, “Hydrodynamic interaction in confined geometries”, J. Phys. Soc. Jpn. **78**, 041002 (2009).

[16] Y. Reyes and Y. Duda, “Modeling of drying in films of colloidal particles”, Langmuir **21**, 7057 (2005).

[17] Q. Liao, L. Chen, X. Qu, and X. Jin, “Brownian dynamics simulation of film formation of mixed polymer latex in the water evaporation stage”, J. Colloid Interface Sci. **227**, 84 (2000).

[18] M. Fujita and Y. Yamaguchi, “Multiscale simulation method for self-organization of nanoparticles in dense suspension”, J. Comput. Phys. **223**, 108 (2007).

[19] M. Fujita and Y. Yamaguchi, “Drying simulation of nanoparticle suspension film on substrate”, in International society of coating science and technology conference (2005).

[20] S. Ohta, S. Inasawa, O. Koike, M. Fujita, and Y. Yamaguchi, “Formation of well-aligned thin films of rod-like nanoparticles via solvent evaporation: a simulation study”, Appl. Phys. Express **2**, 065002 (2009).

[21] D. R. Foss and J. F. Brady, “Brownian dynamics simulation of hard-sphere colloidal dispersions”, J. Rheol. **44**, 629 (2000).

[22] N. Koumakis, M. Laurati, S. U. Egelhaaf, J. F. Brady, and G. Petekidis, “Yielding of hard-sphere glasses during start-up shear”, Phys. Rev. Lett. **108**, 098303 (2012).

[23] N. Koumakis, J. F. Brady, and G. Petekidis, “Complex oscillatory yeilding of model hard-sphere glasses”, Phys. Rev. Lett. **110**, 178301 (2013).

[24] J.-P. Gorce, D. Bovey, P. J. McDonald, P. Palasz, D. Taylor, and J. L. Keddie, “Vertical water distribution during the drying of polymer films cast from aqueous emulsions”, Eur. Phys. J. E Soft Matter **8**, 421 (2002).

[25] T. Narita, P. Hebraud, and F. Lequeux, “Effects of the rate of evaporation and film thickness on nonuniform drying of film-forming concentrated colloidal suspensions”, Eur. Phys. J. E Soft Matter **17**, 69 (2005).

[26] C. M. Cardinal, Y. D. Jung, K. H. Ahn, and L. F. Francis, “Drying regime maps for particulate coatings”, AIChE J. **56**, 2769 (2010).

[27] A. Utgenannt, R. Maspero, A. Fortini, R. Turner, M. Florescu, C. Jeynes, A. G. Kanaras, O. L. Muskens, S. R. P., and J. L. Keddie, “Fast assembly of gold nanoparticles in large-area 2d nanogrids using a one-step, near-infrared radiation-assisted evaporation process”, ACS Nano **10**, 2232 (2016).

[28] P. Pieranski, L. Strzelecki, and B. Pansu, “Thin colloidal crystals”, Phys. Rev. Lett. **50**, 900 (1983).

[29] M. Schmidt and H. Löwen, “Phase diagram of hard spheres confined between two parallel plates”, Phys. Rev. E **55**, 7228 (1997).

[30] A. Fortini and M. Dijkstra, “Phase behaviour of hard spheres confined between parallel hard plates: manipulation of colloidal crystal structures by confinement”, J. Phys.: Condens. Matter **18**, L371 (2006).

[31] J. P. Hansen and I. R. McDonald, *Theory of simple liquids* (Academic Press, 2006).

[32] K. E. Davis, W. B. Russel, and W. J. Glantschnig, “Disorder-to-order transition in settling suspensions of colloidal silica: x-ray measurements”, Science **245**, 507 (1989).

[33] J. P. Hoogenboom, P. Vergeer, and A. van Blaaderen, “A real-space analysis of colloidal crystallization in a gravitational field at a flat bottom wall”, J. Chem. Phys. **119**, 3371 (2003).

[34] C. P. Royall, J. Dzubiella, M. Schmidt, and A. van Blaaderen, “Nonequilibrium sedimentation of colloids on the particle scale”, Phys. Rev. Lett. **98**, 188304 (2007).

[35] T. Biben, R. Ohnesorge, and H. Löwen, “Crystallization in sedimentation profiles of hard spheres”, Europhys. Lett. **28**, 665 (1994).

[36] M. Marechal and M. Dijkstra, “Crystallization of colloidal hard spheres under gravity”, Phys. Rev. E **75**, 061404 (2007).

[37] M. Marechal, M. Hermes, and M. Dijkstra, “Stacking in sediments of colloidal hard spheres”, J. Chem. Phys. **135**, 034510 (2011).

[38] Z.-Q. Li, Z.-Y. Sun, L.-J. An, and Z.-G. Wang, “Heterogeneity in structurally arrested hard spheres”, Europhys. Lett. **84**, 26005 (2008).

[39] R. S. Fishman, E. F. Hill, T. K. Storsved, and G. P. Bierwagen, “Density fluctuations in hard-sphere systems”, J. Appl. Phys. **79**, 729 (1996).

[40] P. N. Segrè, F. Liu, P. Umbanhowar, and D. A. Weitz, “An effective gravitational temperature for sedimentation”, Nature **409**, 594 (2001).

[41] J. N. Israelachvili, “Adhesin forces between surfaces in liquids and condensable vapours”, Surf. Sci. Rep. **14**, 109 (1992).

[42] P. A. Thompson and M. O. Robbins, “Origin of stick-slip motion in boundary lubrication”, Science **250**, 792 (1990).

[43] J.-C. Wang and K. A. Fichthorn, "A method for molecular dynamics simulation of confined fluids", J. Chem. Phys. **112**, 8252 (2000).

[44] H. Eslami, F. Mozaffari, J. Moghadasi, and F. Müller-Plathe, "Molecular dynamics simulation of confined fluids in isosurface-isothermal-isobaric ensemble", J. Chem. Phys. **129**, 194702 (2008).

[45] T. Gruhn and P. A. Monson, "Molecular dynamics simulations of hard sphere solidification at constant pressure", Phys. Rev. E **64**, 061703 (2001).

[46] M. Schoen, D. J. Diestler, and J. H. Cushman, "Shear melting of confined solid monolayer films", Phys. Rev. B **47**, 5603 (1993).

[47] M. Schoen, S. Hess, and D. J. Diestler, "Rheological properties of confined thin films", Phys. Rev. E **52**, 2587 (1995).

[48] A. F. Routh and W. B. Zimmerman, "Distribution of particles during solvent evaporation from films", Chem. Eng. Sci. **59**, 2961 (2004).

[49] G. J. Kynch, "A theory of sedimentation", Trans. Faraday Soc. **48**, 166 (1952).

[50] K. E. Davis and W. B. Russel, "An asymptotic description of transient settling and ultrafiltration of colloidal dispersions", Phys. Fluids A **1**, 82 (1989).

[51] K. Kamrin and G. Koval, "Nonlocal constitutive relation for steady granular flow", Phys. Rev. Lett. **108**, 178301 (2012).

[52] P. Strating, "Brownian dynamics simulation of a hard-sphere suspension", Phys. Rev. E **59**, 2175 (1999).

[53] A. Scala, T. Voigtmann, and C. De Michele, "Event-driven brownian dynamics for hard spheres", J. Chem. Phys. **126**, 134109 (2007).

[54] D. M. Heyes and J. R. Melrose, "Brownian dynamics simulations of model hard-sphere suspensions", J. Non-Newtonian Fluid Mech. **46**, 1 (1993).

[55] B. Cichocki and K. Hinsen, "Dynamic computer simulation of concentrated hard sphere suspensions: i. simulation technique and mean square displacement data", Physica A **166**, 473 (1990).

[56] W. Schaertl and H. Sillescu, "Brownian dynamics simulations of colloidal hard spheres. effects of sample dimensionality on self-diffusion", J. Stat. Phys. **74**, 687 (1994).

[57] D. L. Ermak and J. A. McCammon, "Brownian dynamics with hydrodynamic interactions", J. Chem. Phys. **69**, 1352 (1978).

[58] H. Goldstein, C. P. Poole Jr., and J. L. Safko, *Classical mechanics* (Addison-Wesley, 2001).

[59] C. S. O'Hern, L. E. Silbert, A. J. Liu, and S. R. Nagel, "Jamming at zero temperature and zero applied stress: the epitome of disorder", Phys. Rev. E **68**, 011306 (2003).

[60] E. A. J. F. Peters and T. M. A. O. M. Barenbrug, “Efficient brownian dynamics simulation of particles near walls. i. reflecting and absorbing walls”, Phys. Rev. E **66**, 056701 (2002).

[61] E. J. Le Fevre, “Equation of state for hard-sphere fluid”, Nature Physical Science **235**, 20 (1972).

[62] A. Mulero, ed., *Theory and simulation of hard-sphere fluids and related systems* (Springer, 2008).

[63] P. R. ten Wolde, M. J. Ruiz-Montero, and D. Frenkel, “Numerical evidence for bcc ordering at the surface of a critical fcc nucleus”, Phys. Rev. Lett. **75**, 2714 (1995).

[64] P. J. Steinhardt, D. R. Nelson, and M. Ronchetti, “Bond-orientational order in liquids and glasses”, Phys. Rev. B **28**, 784 (1983).

[65] B. D. Todd, D. J. Evans, and P. J. Daivis, “Pressure tensor for inhomogeneous fluids”, Phys. Rev. E **52**, 1627 (1995).

[66] C. H. Rycroft, “Voro++: a three-dimensional voronoi cell library in c++”, Chaos **19**, 041111 (2009).

[67] J. Crank, *Free and moving boundary problems* (Oxford University Press, 1984).